FLIGHT DYNAMICS AND CONTROL OF A COAXIAL-TEETERING ROTOR ULTRALIGHT HELICOPTER WITH ROTOR-ON-ROTOR INTERACTIONS

Tale Kreienkamp
Visiting M.Sc. Student

Umberto Saetti
Assistant Professor

Department of Aerospace Engineering
University of Maryland
College Park, MD, USA

Süleyman Özkurt
Research Associate

Walter Fichter
Professor

Institute of Flight Mechanics and Controls
University of Stuttgart
Stuttgart, Germany

ABSTRACT

This paper describes the theoretical derivation, implementation, and validation of a teetering rotor model for applications in flight dynamics simulations. The rotor formulation is generic and accounts for both positive and negative angular rotor speeds. The module is integrated within a generic multi-rotor/wing flight dynamics code implemented in MATLAB®/Simulink. The model is validated against flight-identified data for an ultralight coaxial helicopter. The impact of the rotor-on-rotor interactional aerodynamics is evaluated in trimmed flight in terms of spectral and frequency response analyses. Model-order reduction methods are investigated to guide the development of linearized models that are tractable for flight control design while still predicting the effect of rotor-on-rotor interactions on the vehicle flight dynamics. Model-following flight control laws based on these reduced-order linearized models are developed and tested on the nonlinear dynamics. Results indicate that incorporating rotor-on-rotor aerodynamic interactions significantly affects trim, dynamic response, and power requirements. These interactions introduce nonzero roll trim attitudes and increased collective and pedal inputs at low speeds due to asymmetric thrust distribution between rotors. The upper rotor generates higher thrust and inflow while the lower rotor operates in its wake, leading to over 60% higher total power consumption. Frequency response analysis shows improved gain and phase alignment with flight-identified data, particularly in roll, yaw, and heave responses above 0.4–0.5 rad/s.

INTRODUCTION

The flight dynamics of a coaxial helicopter differ significantly from those of a conventional single main–tail rotor helicopter. For example, while the heave and yaw dynamics of conventional helicopters are strongly coupled due to the torque generated by the main rotor, this coupling is largely absent in coaxial helicopters, where the counter-rotating rotors approximately cancel each other's torque. This not only reduces inter-axis coupling, but also allows coaxial configurations to be trimmed with approximately zero sideslip and bank angle. Conventional helicopters, on the other hand, must typically be trimmed for either zero sideslip or zero bank angle, but not both simultaneously. The coaxial helicopter considered in this study features a teetering rotor system without a flapping hinge, resulting in a non-dimensional flapping frequency of one-per-revolution (1/rev), as noted in (Ref. 1). The rotor therefore operates at resonance, and the blade flapping response lags the cyclic control input by 90 degrees – consistent with the behavior of second – order systems at resonance. Consequently, there is no need for swashplate phasing, which is typically used in articulated rotors to mitigate the roll–pitch cross-coupling induced by flapping hinge offset. These characteristics may provide operational advantages over conventional configurations, particularly for novice or recreational pilots, who often require extended training to achieve proficiency in rotorcraft control.

As an ultralight rotorcraft, the coaxial helicopter considered in this study offers advantages in terms of reduced maintenance requirements and mechanical simplicity compared to conventional designs. However, several flight dynamic challenges – some common to most hovering vehicles – remain. Prior studies (Refs. 2, 3), as well as the analysis by McRuer (Ref. 4), have identified coupled pitch–roll instabilities in hover, which can pose significant handling challenges, particularly for less experienced pilots. To improve stability and controllability, the implementation of a stability and control augmentation system (SCAS) is warranted. The development of such a system requires an accurate flight dynamics model that captures rotor-on-rotor aerodynamic interactions. This model may be obtained through system identification based on flight test data or derived from a first-principles, physics-based formulation. Given the cost and complexity of flight testing, as well as its applicability primarily to existing airframes rather than early-stage design evaluations, a physics-based model is particularly valuable for stability analysis, handling-quality assessment, and flight control system development.

Previous work on coaxial rotorcraft, particularly the edm aerotec CoAX 600 platform, has primarily focused on control-oriented modeling and parameter estimation. In Ref. 5, Hosseini et al. developed a nonlinear simulation model using blade element momentum theory (BEMT), which was coupled with a rigid-body fuselage model and used for control design and validation. Unknown aerodynamic and inertial parameters were identified using maximum likelihood estimation based on flight test data. The model was validated in both time and frequency domains, and linearizations were employed for control law synthesis. Follow-up studies (Refs. 6–8) extended this approach to include a finite-state dynamic inflow model and expanded parameter estimation to forward flight. While these contributions represent important progress toward dynamic modeling of coaxial rotorcraft, the resulting models remain partially empirical and do not resolve the rotor–rotor aerodynamic interactions or nonlinear kinematics inherent to teetering rotor systems. To date, a comprehensive, physics-based model that captures the flight mechanics of a coaxial teetering rotor system system with rotor-on-rotor interactions has yet to be developed.

Accordingly, the objectives of this study are as follows: (i) develop a generic flight dynamics model of the ultralight coaxial helicopter shown in Fig. 1, ensuring linearizability and incorporating a teetering rotor system, and rotor-on-rotor aerodynamic interactions, building upon previous work (Refs. 9, 10); (ii) assess the impact of rotor-on-rotor interactional aerodynamics on flight dynamics; (iii) investigate model-order reduction techniques to generate linearized representations suitable for flight control design while preserving the key aerodynamic interactions affecting flight dynamics; and (iv) implement and evaluate model-following flight control laws based on reduced-order models, demonstrating their effectiveness in nonlinear simulations in meeting desired stability, response, and handling-quality criteria.

Figure 1: Ultralight coaxial helicopter to be modeled generically. Source: EDM Aerotec GmbH (Ref. 11).

Specific novelties of this work include: (i) the development of a teetering rotor model for flight dynamics applications; (ii) the development of a physics-based model of the current teetering coaxial rotorcraft that accounts for rotor-on-rotor interactions; and (iii) the design of an automatic flight control system (AFCS) for this configuration, based on linearized models that incorporate rotor-on-rotor aerodynamic effects.

The paper is organized as follows. It begins with the theoretical derivation and formulation of a teetering rotor model intended for flight dynamics simulation, capable of handling both positive and negative rotor angular velocities. The implementation of this model within a generic multi-rotor/wing flight dynamics framework in MATLAB®/Simulink is then described. Validation is performed against flight-identified data for an ultralight coaxial helicopter. The influence of rotor-on-rotor aerodynamic interactions is examined in trimmed flight through spectral and frequency response analyses. Subsequently, model-order reduction techniques are explored to generate linearized representations suitable for flight control design while preserving the effects of rotor-on-rotor coupling. Finally, model-following flight control laws are developed based on the reduced-order models and evaluated within the full nonlinear simulation environment.

TEETERING ROTOR MODEL

Transformation Matrices

As the base for the kinematics and dynamics derivations that follow, it is convenient to introduce commonly-used transformations between reference frames.

Body to Hub Frame Transformation Consider Fig. 2. In the present analysis, rotor hub tilt is defined as positive aft, while hub cant is defined as positive for right-wing-down orientation. The rotor hub frame, labeled H, is related to the body frame through two successive transformations. The first transformation is a rotation about the $\boldsymbol{i}_B$ axis by an angle ϕ_m, resulting in the intermediate frame T (Fig. 3a).

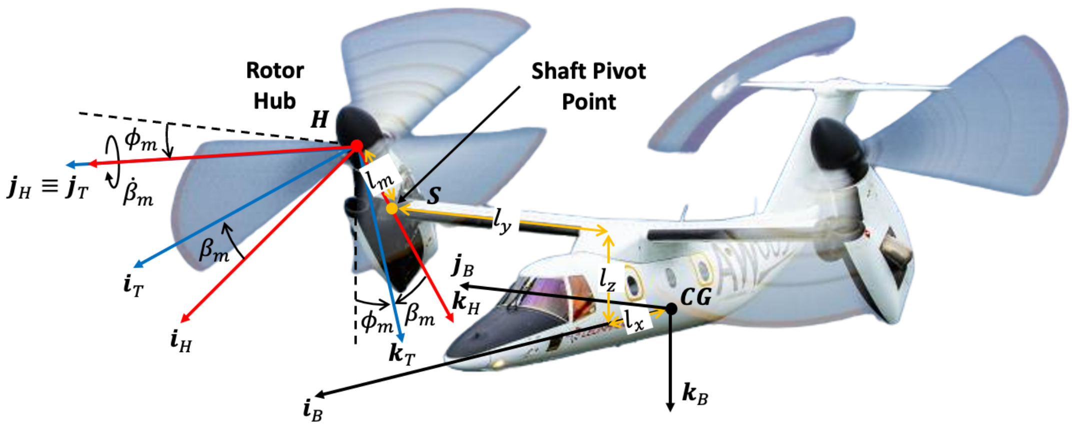

Figure 2: Rotor hub cant and tilt angles on a AW609.

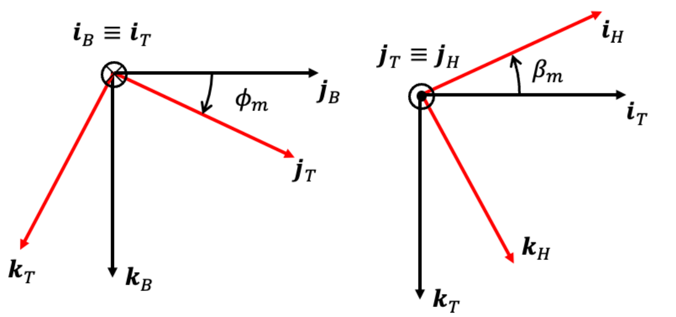

(a) Rotation about the $\boldsymbol{i}_B$ axis by an angle ϕ_m.

(b) Rotation about the $\boldsymbol{j}_T$ axis by an angle β_m.

Figure 3: Body to hub frame rotations.

$$\begin{bmatrix} \boldsymbol{i}_T \\ \boldsymbol{j}_T \\ \boldsymbol{k}_T \end{bmatrix} = \underbrace{\begin{bmatrix} 1 & 0 & 0 \\ 0 & c_{\phi_m} & s_{\phi_m} \\ 0 & -s_{\phi_m} & c_{\phi_m} \end{bmatrix}}_{\boldsymbol{T}_{B\to T}} \begin{bmatrix} \boldsymbol{i}_B \\ \boldsymbol{j}_B \\ \boldsymbol{k}_B \end{bmatrix} \tag{1}$$

Note that, according to this definition, main rotors with a rotation axis aligned with the $\boldsymbol{k}_B$ axis have a cant angle of $\phi_m = 0$ deg. Conversely, tail rotors with a rotation axis aligned with the $\boldsymbol{j}_B$ axis have a cant angle of $\phi_m = 90$ deg. The second transformation is a rotation about the $\boldsymbol{j}_T$ axis by an angle β_m, resulting in the hub frame H (Fig. 3b).

$$\begin{bmatrix} \boldsymbol{i}_H \\ \boldsymbol{j}_H \\ \boldsymbol{k}_H \end{bmatrix} = \underbrace{\begin{bmatrix} c_{\beta_m} & 0 & -s_{\beta_m} \\ 0 & 1 & 0 \\ s_{\beta_m} & 0 & c_{\beta_m} \end{bmatrix}}_{\boldsymbol{T}_{T\to H}} \begin{bmatrix} \boldsymbol{i}_T \\ \boldsymbol{j}_T \\ \boldsymbol{k}_T \end{bmatrix} \tag{2}$$

According to this definition, the tilt angle of either rotor of a tiltrotor aircraft in helicopter mode is $\beta_m = 0$ deg. Conversely, in airplane mode, the tilt angle is $\beta_m = -90$ deg. Similarly, the forward tilt of the UH-60 main rotor is represented as $\beta_m = -3$ deg. The transformation from the body frame to the hub frame is obtained by substituting Eq. (2) into Eq. (1).

$$\begin{aligned} \begin{bmatrix} \boldsymbol{i}_H \\ \boldsymbol{j}_H \\ \boldsymbol{k}_H \end{bmatrix} &= \boldsymbol{T}_{T\to H}\boldsymbol{T}_{B\to T} \begin{bmatrix} \boldsymbol{i}_B \\ \boldsymbol{j}_B \\ \boldsymbol{k}_B \end{bmatrix} \\ &= \underbrace{\begin{bmatrix} c_{\beta_m} & s_{\beta_m}s_{\phi_m} & -s_{\beta_m}c_{\phi_m} \\ 0 & c_{\phi_m} & s_{\phi_m} \\ s_{\beta_m} & -c_{\beta_m}s_{\phi_m} & c_{\beta_m}c_{\phi_m} \end{bmatrix}}_{\boldsymbol{T}_{B\to H}} \begin{bmatrix} \boldsymbol{i}_B \\ \boldsymbol{j}_B \\ \boldsymbol{k}_B \end{bmatrix} \end{aligned} \tag{3}$$

The inverse transformation, *i.e.*, that from the hub to the body frame, is:

$$\begin{aligned} \begin{bmatrix} \boldsymbol{i}_B \\ \boldsymbol{j}_B \\ \boldsymbol{k}_B \end{bmatrix} &= \boldsymbol{T}_{B\to H}^T \begin{bmatrix} \boldsymbol{i}_H \\ \boldsymbol{j}_H \\ \boldsymbol{k}_H \end{bmatrix} \\ &= \underbrace{\begin{bmatrix} c_{\beta_m} & 0 & s_{\beta_m} \\ s_{\beta_m}s_{\phi_m} & c_{\phi_m} & -c_{\beta_m}s_{\phi_m} \\ -s_{\beta_m}c_{\phi_m} & s_{\phi_m} & c_{\beta_m}c_{\phi_m} \end{bmatrix}}_{\boldsymbol{T}_{H\to B}} \begin{bmatrix} \boldsymbol{i}_H \\ \boldsymbol{j}_H \\ \boldsymbol{k}_H \end{bmatrix} \end{aligned} \tag{4}$$

Hub to Blade Frame Transformation Consider a teetering rotor blade, as shown in Fig. 4.

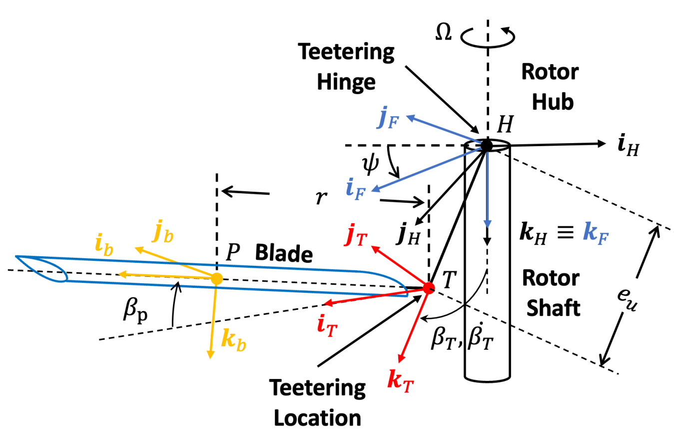

Figure 4: Teetering rotor schematics.

The blade undergoes the following motion (successive single-axis rotations), shown in Fig. 5:

1. Rotation with an angular speed $-\Omega$ about the vertical axis of the rotor hub frame $\boldsymbol{k}_H$. The degree of freedom associated to this rotation is the azimuth angle ψ. The transformation from the hub to the flap frame is:

$$\begin{bmatrix} \boldsymbol{i}_F \\ \boldsymbol{j}_F \\ \boldsymbol{k}_F \end{bmatrix} = \begin{bmatrix} c_{(\pi-\psi)} & s_{(\pi-\psi)} & 0 \\ -s_{(\pi-\psi)} & c_{(\pi-\psi)} & 0 \\ 0 & 0 & 1 \end{bmatrix} \begin{bmatrix} \boldsymbol{i}_H \\ \boldsymbol{j}_H \\ \boldsymbol{k}_H \end{bmatrix} = \underbrace{\begin{bmatrix} -c_\psi & s_\psi & 0 \\ -s_\psi & -c_\psi & 0 \\ 0 & 0 & 1 \end{bmatrix}}_{\boldsymbol{T}_{H\to F}} \begin{bmatrix} \boldsymbol{i}_H \\ \boldsymbol{j}_H \\ \boldsymbol{k}_H \end{bmatrix} \tag{5}$$

2. Rotation about the $\boldsymbol{k}_F$ axis, of the teetering angle β_T and with a flap rate $\dot{\beta}_T$. The transformation from the flap to the teetering frame is:

$$\begin{bmatrix} \boldsymbol{i}_T \\ \boldsymbol{j}_T \\ \boldsymbol{k}_T \end{bmatrix} = \underbrace{\begin{bmatrix} c_{\beta_T} & 0 & -s_{\beta_T} \\ 0 & 1 & 0 \\ s_{\beta_T} & 0 & c_{\beta_T} \end{bmatrix}}_{\boldsymbol{T}_{F\to T}} \begin{bmatrix} \boldsymbol{i}_F \\ \boldsymbol{j}_F \\ \boldsymbol{k}_F \end{bmatrix} \tag{6}$$

3. Rotation about the $\boldsymbol{j}_T$ axis of an angle β_p, where β_p is the *precone* angle. Both of these quantities are fixed. The transformation from the teetering to the blade frame is:

$$\begin{bmatrix} \boldsymbol{i}_b \\ \boldsymbol{j}_b \\ \boldsymbol{k}_b \end{bmatrix} = \underbrace{\begin{bmatrix} c_{\beta_p} & 0 & -s_{\beta_p} \\ 0 & 1 & 0 \\ s_{\beta_p} & 0 & c_{\beta_p} \end{bmatrix}}_{\boldsymbol{T}_{T\to b}} \begin{bmatrix} \boldsymbol{i}_T \\ \boldsymbol{j}_T \\ \boldsymbol{k}_T \end{bmatrix} \tag{7}$$

Because the second and third transformations are conducted about parallel axes $\boldsymbol{j}_F$ and $\boldsymbol{j}_T$, it is convenient to express these rotations as a single transformation. As such, the transformation between the hub and the teetering frame can be found by substituting Eq. (7) into Eq. (6):

$$\begin{aligned} \begin{bmatrix} \boldsymbol{i}_b \\ \boldsymbol{j}_b \\ \boldsymbol{k}_b \end{bmatrix} &= \boldsymbol{T}_{T\to b}\boldsymbol{T}_{F\to T} \begin{bmatrix} \boldsymbol{i}_F \\ \boldsymbol{j}_F \\ \boldsymbol{k}_F \end{bmatrix} \\ &= \begin{bmatrix} c_{(\beta_T+\beta_p)} & 0 & -s_{(\beta_T+\beta_p)} \\ 0 & 1 & 0 \\ s_{(\beta_T+\beta_p)} & 0 & c_{(\beta_T+\beta_p)} \end{bmatrix} \begin{bmatrix} \boldsymbol{i}_F \\ \boldsymbol{j}_F \\ \boldsymbol{k}_F \end{bmatrix} \\ &= \underbrace{\begin{bmatrix} c_\beta & 0 & -s_\beta \\ 0 & 1 & 0 \\ s_\beta & 0 & c_\beta \end{bmatrix}}_{\boldsymbol{T}_{F\to b}} \begin{bmatrix} \boldsymbol{i}_F \\ \boldsymbol{j}_F \\ \boldsymbol{k}_F \end{bmatrix} \end{aligned} \tag{8}$$

where $\beta = \beta_T + \beta_p$ is the total flapping angle, which accounts for both teetering rotation and precone. Note that because β_p is a constant, $\dot{\beta} = \dot{\beta}_T$. The transformation from the hub to the blade frame is found by substituting Eq. (5) into Eq. (8):

$$\begin{aligned} \begin{bmatrix} \boldsymbol{i}_b \\ \boldsymbol{j}_b \\ \boldsymbol{k}_b \end{bmatrix} &= \boldsymbol{T}_{F\to b}\boldsymbol{T}_{H\to F} \begin{bmatrix} \boldsymbol{i}_H \\ \boldsymbol{j}_H \\ \boldsymbol{k}_H \end{bmatrix} \\ &= \underbrace{\begin{bmatrix} -c_\psi c_\beta & s_\psi c_\beta & -s_\beta \\ -s_\psi & -c_\psi & 0 \\ -c_\psi s_\beta & s_\psi s_\beta & c_\beta \end{bmatrix}}_{\boldsymbol{T}_{H\to b}} \begin{bmatrix} \boldsymbol{i}_H \\ \boldsymbol{j}_H \\ \boldsymbol{k}_H \end{bmatrix} \end{aligned} \tag{9}$$

The inverse transformation, *i.e.*, that from the blade to the hub frame, is:

$$\begin{bmatrix} \boldsymbol{i}_H \\ \boldsymbol{j}_H \\ \boldsymbol{k}_H \end{bmatrix} = \boldsymbol{T}_{H\to b}^T \begin{bmatrix} \boldsymbol{i}_b \\ \boldsymbol{j}_b \\ \boldsymbol{k}_b \end{bmatrix} = \underbrace{\begin{bmatrix} -c_\psi c_\beta & -s_\psi & -c_\psi s_\beta \\ s_\psi c_\beta & -c_\psi & s_\psi s_\beta \\ -s_\beta & 0 & c_\beta \end{bmatrix}}_{\boldsymbol{T}_{b\to H}} \begin{bmatrix} \boldsymbol{i}_b \\ \boldsymbol{j}_b \\ \boldsymbol{k}_b \end{bmatrix} \tag{10}$$

Another useful rotation is that from the hub to the teetering frame, which can be found by substituting Eq. (5) into Eq.

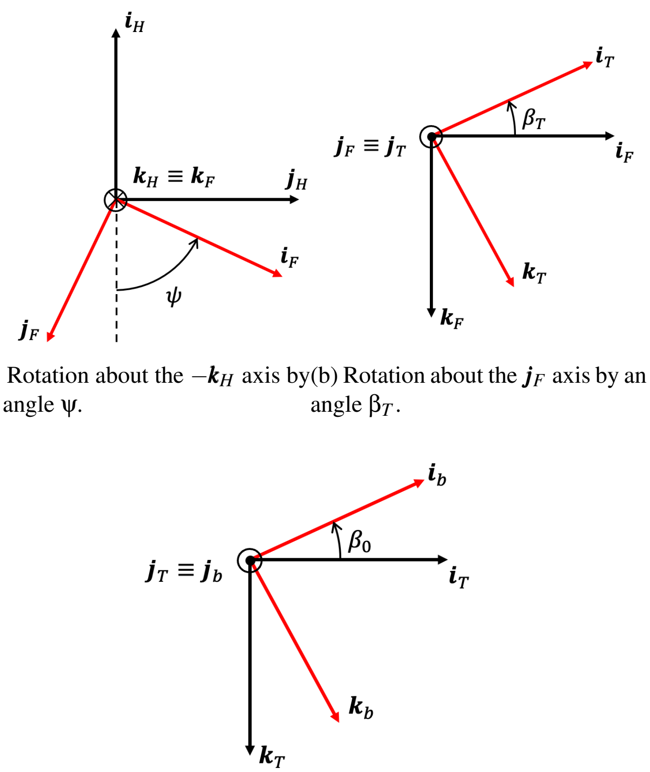

(a) Rotation about the $-\boldsymbol{k}_H$ axis by an angle ψ.

(b) Rotation about the $\boldsymbol{j}_F$ axis by an angle β_T.

(c) Rotation about the $\boldsymbol{j}_T$ axis by an angle β_p.

Figure 5: Rotor hub to blade frame rotations.

(6):

$$\begin{aligned}\begin{bmatrix}\boldsymbol{i}_T\\ \boldsymbol{j}_T\\ \boldsymbol{k}_T\end{bmatrix} &= \boldsymbol{T}_{F\to T}\boldsymbol{T}_{H\to F}\begin{bmatrix}\boldsymbol{i}_H\\ \boldsymbol{j}_H\\ \boldsymbol{k}_H\end{bmatrix}\\ &= \underbrace{\begin{bmatrix}-c_\psi c_{\beta_T} & s_\psi c_{\beta_T} & -s_{\beta_T}\\ -s_\psi & -c_\psi & 0\\ -c_\psi s_{\beta_T} & s_\psi s_{\beta_T} & c_{\beta_T}\end{bmatrix}}_{\boldsymbol{T}_{H\to T}}\begin{bmatrix}\boldsymbol{i}_H\\ \boldsymbol{j}_H\\ \boldsymbol{k}_H\end{bmatrix}\end{aligned} \tag{11}$$

The inverse transformation, *i.e.*, that from the teetering to the hub frame, is:

$$\begin{bmatrix}\boldsymbol{i}_H\\ \boldsymbol{j}_H\\ \boldsymbol{k}_H\end{bmatrix} = \boldsymbol{T}^T_{H\to T}\begin{bmatrix}\boldsymbol{i}_T\\ \boldsymbol{j}_T\\ \boldsymbol{k}_T\end{bmatrix} = \underbrace{\begin{bmatrix}-c_\psi c_{\beta_T} & -s_\psi & -c_\psi s_{\beta_T}\\ s_\psi c_{\beta_T} & -c_\psi & s_\psi s_{\beta_T}\\ -s_{\beta_T} & 0 & c_{\beta_T}\end{bmatrix}}_{\boldsymbol{T}_{T\to H}}\begin{bmatrix}\boldsymbol{i}_T\\ \boldsymbol{j}_T\\ \boldsymbol{k}_T\end{bmatrix} \tag{12}$$

Blade to Air Mass Frame Transformation When calculating the lift and drag of an airfoil section, lift and drag are defined as the components perpendicular and parallel, respectively, to the velocity vector of the air mass through which the blade section is moving. The air mass frame is obtained by a positive rotation about the radial axis $\boldsymbol{i}_a$ through an angle of $\pi-\phi$, where ϕ is the inflow angle, to be defined later in the article. The transformation from the blade frame to the air mass frame is given by:

$$\begin{aligned}\begin{bmatrix}\boldsymbol{i}_a\\ \boldsymbol{j}_a\\ \boldsymbol{k}_a\end{bmatrix} &= \begin{bmatrix}1 & 0 & 0\\ 0 & c_{(\pi-\phi)} & s_{(\pi-\phi)}\\ 0 & -s_{(\pi-\phi)} & c_{(\pi-\phi)}\end{bmatrix}\begin{bmatrix}\boldsymbol{i}_b\\ \boldsymbol{j}_b\\ \boldsymbol{k}_b\end{bmatrix}\\ &= \underbrace{\begin{bmatrix}1 & 0 & 0\\ 0 & -c_\phi & s_\phi\\ 0 & -s_\phi & -c_\phi\end{bmatrix}}_{\boldsymbol{T}_{b\to a}}\begin{bmatrix}\boldsymbol{i}_b\\ \boldsymbol{j}_b\\ \boldsymbol{k}_b\end{bmatrix}\end{aligned} \tag{13}$$

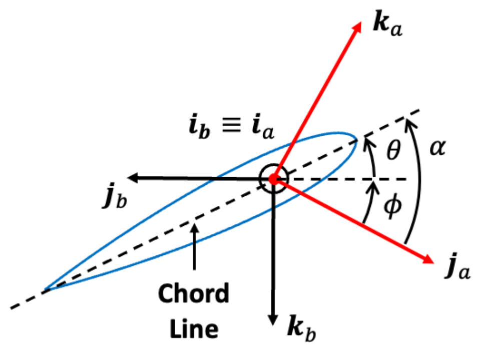

Figure 6: Transformation from the blade to the air mass frame.

Blade to Radial-Tangential-Perpendicular Frame Transformation For aerodynamic calculations, it is convenient to reverse the direction of the $\boldsymbol{j}_b$ axis of the blade frame to obtain the radial–tangential–perpendicular (RTP) frame. Note that the RTP frame is a left-handed coordinate system. The transformation from the blade frame to the RTP frame, shown in Fig. 7, is given by:

$$\begin{bmatrix}\boldsymbol{R}\\ \boldsymbol{T}\\ \boldsymbol{P}\end{bmatrix} = \underbrace{\begin{bmatrix}1 & 0 & 0\\ 0 & -1 & 0\\ 0 & 0 & 1\end{bmatrix}}_{\boldsymbol{T}_{b\to RTP}}\begin{bmatrix}\boldsymbol{i}_b\\ \boldsymbol{j}_b\\ \boldsymbol{k}_b\end{bmatrix} = \begin{bmatrix}\boldsymbol{i}_b\\ -\boldsymbol{j}_b\\ \boldsymbol{k}_b\end{bmatrix} \tag{14}$$

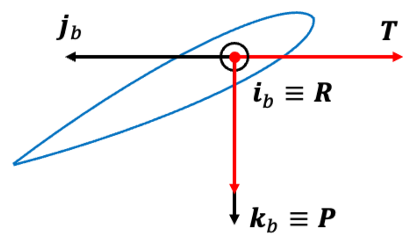

Figure 7: Transformation from the blade to the RTP frame.

Blade Kinematics

Blade Element Position It may be useful to know the positions of the blade elements for either visualization purposes, or to interpolate velocity perturbations at each blade element. Assume the position vector from the rotor hub to the teetering location to be $\boldsymbol{r}^T_{H\to T} = e_u R \boldsymbol{k}_T$, where e_u is the *undersling* distance non-dimensionalized by the rotor radius R. Additionally, assume the position vector from the teetering location T to an arbitrary point P on the blade to be $\boldsymbol{r}^b_{T\to P} = r\boldsymbol{i}_b$, where r is the blade dimensional radial coordinate. Then, the position vector from the hub frame origin to the blade element, expressed in the hub frame:

$$\begin{aligned}\boldsymbol{r}^H_{H\to P} =& \boldsymbol{r}^H_{H\to T} + \boldsymbol{r}^H_{T\to P}\\ =& \boldsymbol{T}_{T\to H}\boldsymbol{r}^T_{H\to T} + \boldsymbol{T}_{b\to H}\boldsymbol{r}^b_{T\to P}\\ =& \begin{bmatrix}-c_\psi c_{\beta_T} & -s_\psi & -c_\psi s_{\beta_T}\\ s_\psi c_{\beta_T} & -c_\psi & s_\psi s_{\beta_T}\\ -s_{\beta_T} & 0 & c_{\beta_T}\end{bmatrix}\begin{bmatrix}0\\ 0\\ e_u R\end{bmatrix}\\ &+ \begin{bmatrix}-c_\psi c_\beta & -s_\psi & -c_\psi s_\beta\\ s_\psi c_\beta & -c_\psi & s_\psi s_\beta\\ -s_\beta & 0 & c_\beta\end{bmatrix}\begin{bmatrix}r\\ 0\\ 0\end{bmatrix}\\ =& \begin{bmatrix}-c_\psi\left(e_u R s_{\beta_T} + r c_\beta\right)\\ s_\psi\left(e_u R s_{\beta_T} + r c_\beta\right)\\ e_u R c_{\beta_T} - r s_\beta\end{bmatrix}\end{aligned} \tag{15}$$

The position vector from the origin of the inertial frame to the blade element, expressed in inertial-frame components, is:

$$\begin{aligned}\boldsymbol{r}^I_{O\to b} =& \boldsymbol{r}^I_{O\to\oplus} + \boldsymbol{T}_{B\to I}\boldsymbol{r}^B_{\oplus\to H} + \boldsymbol{r}^I_{H\to P}\\ =& \boldsymbol{r}^I_{O\to\oplus} + \boldsymbol{T}_{B\to I}\boldsymbol{r}^B_{\oplus\to H} + \boldsymbol{T}_{B\to I}\boldsymbol{T}_{H\to B}\boldsymbol{r}^H_{H\to P}\\ =& \begin{bmatrix}x\\ y\\ z\end{bmatrix} + \boldsymbol{T}_{B\to I}\begin{bmatrix}x_H\\ y_H\\ z_H\end{bmatrix}\\ &+ \boldsymbol{T}_{B\to I}\boldsymbol{T}_{H\to B}\begin{bmatrix}-c_\psi\left(e_u R s_{\beta_T} + r c_\beta\right)\\ s_\psi\left(e_u R s_{\beta_T} + r c_\beta\right)\\ e_u R c_{\beta_T} - r s_\beta\end{bmatrix} = \begin{bmatrix}x_b\\ y_b\\ z_b\end{bmatrix}\end{aligned} \tag{16}$$

Blade Element Velocity The velocity of the teetering location with respect to the inertial frame, expressed in the hub frame, is:

$$
\begin{aligned}
\boldsymbol{v}^H_{T/I} =& \boldsymbol{v}^H_{H/I} + \boldsymbol{\omega}^H_{T/I} \times \boldsymbol{r}^H_{H\to T}\\
=& \boldsymbol{v}^H_{H/I} + \left(\boldsymbol{T}_{F\to H}\boldsymbol{\omega}^F_{T/F} + \boldsymbol{\omega}^H_{F/H} + \boldsymbol{\omega}^H_{H/I}\right) \times \left(\boldsymbol{T}_{T\to H}\boldsymbol{r}^T_{H\to T}\right)\\
=& \begin{bmatrix} u_H \\ v_H \\ w_H \end{bmatrix} + \left(\boldsymbol{T}_{F\to H}\begin{bmatrix} 0 \\ \dot{\beta} \\ 0 \end{bmatrix} + \begin{bmatrix} 0 \\ 0 \\ -\Omega \end{bmatrix} + \begin{bmatrix} p_H \\ q_H \\ r_H \end{bmatrix}\right)\\
& \times \left(\boldsymbol{T}_{T\to H}\begin{bmatrix} 0 \\ 0 \\ e_u R \end{bmatrix}\right)\\
=& \begin{bmatrix} u_H \\ v_H \\ w_H \end{bmatrix} + \begin{bmatrix} -\dot{\beta}s_\psi + p_H \\ -\dot{\beta}c_\psi + q_H \\ r_H - \Omega \end{bmatrix} \times \begin{bmatrix} -e_u R c_\psi s_{\beta_T} \\ e_u R s_\psi s_{\beta_T} \\ e_u R c_{\beta_T} \end{bmatrix}\\
=& \begin{bmatrix} u_H + e_u R\left[c_{\beta_T}\left(q_H - \dot{\beta}c_\psi\right) - \omega_z s_\psi s_{\beta_T}\right] \\ v_H - e_u R\left[c_{\beta_T}\left(p_H - \dot{\beta}s_\psi\right) + \omega_z c_\psi s_{\beta_T}\right] \\ w_H - e_u R s_{\beta_T}\left(\dot{\beta} + \omega_y\right) \end{bmatrix} = \begin{bmatrix} u_T \\ v_T \\ w_T \end{bmatrix}
\end{aligned}
\tag{17}
$$

The velocity of the blade element with respect to the inertial frame, expressed in blade-frame components, is:

$$
\begin{aligned}
\boldsymbol{v}^b_{P/I} =& \boldsymbol{v}^b_{T/I} + \boldsymbol{\omega}^b_{b/I} \times \boldsymbol{r}^b_{T\to P}\\
=& \boldsymbol{T}_{H\to b}\boldsymbol{v}^H_{T/I} + \left(\boldsymbol{\omega}^b_{T/F} + \boldsymbol{\omega}^b_{F/H} + \boldsymbol{\omega}^b_{H/I}\right) \times \boldsymbol{r}^b_{T\to P}\\
=& \boldsymbol{T}_{H\to b}\boldsymbol{v}^H_{T/I}\\
& + \left[\boldsymbol{T}_{T\to b}\boldsymbol{\omega}^T_{T/F} + \boldsymbol{T}_{H\to b}\left(\boldsymbol{\omega}^H_{F/H} + \boldsymbol{\omega}^H_{H/I}\right)\right] \times \boldsymbol{r}^b_{T\to P}\\
=& \boldsymbol{T}_{H\to b}\begin{bmatrix} u_T \\ v_T \\ w_T \end{bmatrix} + \left(\begin{bmatrix} 0 \\ \dot{\beta} \\ 0 \end{bmatrix} + \boldsymbol{T}_{H\to b}\begin{bmatrix} p_H \\ q_H \\ r_H - \Omega \end{bmatrix}\right) \times \begin{bmatrix} r \\ 0 \\ 0 \end{bmatrix}\\
=& \begin{bmatrix} u_b \\ v_b \\ w_b \end{bmatrix}
\end{aligned}
\tag{18}
$$

where:

$$u_b = -u_H c_\psi c_\beta + v_H s_\psi c_\beta - w_H s_\beta + e_u R c_{\beta_p}\left(\dot{\beta} + \omega_y\right) \tag{19a}$$

$$
\begin{aligned}
v_b =& -u_H s_\psi - v_H c_\psi + r\left(\omega_x s_\beta + \omega_z c_\beta\right)\\
& + e_u R\left(-\omega_x c_{\beta_T} + \omega_z s_{\beta_T}\right)
\end{aligned}
\tag{19b}
$$

$$w_b = -u_H c_\psi s_\beta + v_H s_\psi s_\beta + w_H c_\beta + \left(e_u R s_{\beta_p} - r\right)\left(\dot{\beta} + \omega_y\right) \tag{19c}$$

Recall that ω_x, ω_y, and ω_z are the components of the angular velocity of the hub frame with respect to the inertial frame expressed in the rotating frame:

$$
\begin{aligned}
\boldsymbol{\omega}^F_{H/I} &= \boldsymbol{\omega}^F_{F/H} + \boldsymbol{\omega}^F_{H/I}\\
&= \boldsymbol{\omega}^F_{F/H} + \boldsymbol{T}_{H\to F}\boldsymbol{\omega}^H_{H/I}\\
&= \begin{bmatrix} 0 \\ 0 \\ -\Omega \end{bmatrix} + \begin{bmatrix} -c_\psi & s_\psi & 0 \\ -s_\psi & -c_\psi & 0 \\ 0 & 0 & 1 \end{bmatrix}\begin{bmatrix} p_H \\ q_H \\ r_H \end{bmatrix}\\
&= \begin{bmatrix} -p_H c_\psi + q_H s_\psi \\ -p_H s_\psi - q_H c_\psi \\ r_H - \Omega \end{bmatrix} = \begin{bmatrix} \omega_x \\ \omega_y \\ \omega_z \end{bmatrix}
\end{aligned}
\tag{20}
$$

Blade Element Acceleration The acceleration of the blade element with respect to the inertial frame, expressed in blade-frame components, can be found via the vector derivative transport theorem:

$$
\begin{aligned}
\boldsymbol{a}^b_{P/I} =& \mathrm{I}\,\frac{d}{dt}\left(\boldsymbol{v}^b_{P/I}\right)\\
=& \mathrm{b}\,\frac{d}{dt}\left(\boldsymbol{v}^b_{P/I}\right) + \boldsymbol{\omega}^b_{b/I} \times \boldsymbol{v}^b_{P/I}\\
=& \mathrm{b}\,\frac{d}{dt}\left(\boldsymbol{v}^b_{P/I}\right)\\
& + \left[\boldsymbol{T}_{T\to b}\boldsymbol{\omega}^T_{T/F} + \boldsymbol{T}_{H\to b}\left(\boldsymbol{\omega}^H_{F/H} + \boldsymbol{\omega}^H_{H/I}\right)\right] \times \boldsymbol{v}^b_{P/I}\\
=& \mathrm{b}\,\frac{d}{dt}\left(\boldsymbol{v}^b_{P/I}\right)\\
& - \boldsymbol{v}^b_{P/I} \times \left[\boldsymbol{T}_{T\to b}\boldsymbol{\omega}^T_{T/F} + \boldsymbol{T}_{H\to b}\left(\boldsymbol{\omega}^H_{F/H} + \boldsymbol{\omega}^H_{H/I}\right)\right]\\
=& \begin{bmatrix} \dot{u}_b \\ \dot{v}_b \\ \dot{w}_b \end{bmatrix} - \begin{bmatrix} u_b \\ v_b \\ w_b \end{bmatrix} \times \left(\begin{bmatrix} 0 \\ \dot{\beta} \\ 0 \end{bmatrix} + \boldsymbol{T}_{H\to b}\begin{bmatrix} p_H \\ q_H \\ r_H - \Omega \end{bmatrix}\right)\\
=& \begin{bmatrix} \dot{u}_b \\ \dot{v}_b \\ \dot{w}_b \end{bmatrix} - \begin{bmatrix} 0 & -w_b & v_b \\ w_b & 0 & -u_b \\ -v_b & u_b & 0 \end{bmatrix}\begin{bmatrix} \omega_x c_\beta - \omega_z s_\beta \\ \dot{\beta} + \omega_y \\ \omega_x s_\beta + \omega_z c_\beta \end{bmatrix}\\
=& \begin{bmatrix} a_x \\ a_y \\ a_z \end{bmatrix}
\end{aligned}
\tag{21}
$$

The time derivatives of the blade element velocities expressed in the blade frame are:

$$
\begin{aligned}
\dot{u}_b = & -\dot{u}_H c_\psi c_\beta + u_H s_\psi c_\beta \Omega + u_H c_\psi s_\beta \dot{\beta} \\
& + \dot{v}_H s_\psi c_\beta + v_H c_\psi c_\beta \Omega - v_H s_\psi s_\beta \dot{\beta} \\
& - \dot{w}_H s_\beta - w_H c_\beta \dot{\beta} \\
& + e_u R c_{\beta_p} \left(\ddot{\beta} + \dot{\omega}_y \right)
\end{aligned} \tag{22a}
$$

$$
\begin{aligned}
\dot{v}_b = & -\dot{u}_H s_\psi - u_H c_\psi \Omega \\
& - \dot{v}_H c_\psi + v_H s_\psi \Omega \\
& + r \left(\dot{\omega}_x s_\beta + \omega_x \dot{\beta} c_\beta + \dot{\omega}_z c_\beta - \omega_z \dot{\beta} s_\beta \right) \\
& + e_u R \left(-\dot{\omega}_x c_{\beta_T} + \omega_x \dot{\beta} s_{\beta_T} + \dot{\omega}_z s_{\beta_T} + \omega_z \dot{\beta} c_{\beta_T} \right)
\end{aligned} \tag{22b}
$$

$$
\begin{aligned}
\dot{w}_b = & -\dot{u}_H c_\psi s_\beta + u_H s_\psi s_\beta \Omega - u_H c_\psi c_\beta \dot{\beta} \\
& + \dot{v}_H s_\psi s_\beta + v_H c_\psi s_\beta \Omega + v_H s_\psi c_\beta \dot{\beta} \\
& + \dot{w}_H c_\beta - w_H s_\beta \dot{\beta} \\
& + \left(e_u R s_{\beta_p} - r \right) \left(\ddot{\beta} + \dot{\omega}_y \right)
\end{aligned} \tag{22c}
$$

Then, the blade element accelerations, expressed in the blade frame, will be:

$$
\begin{aligned}
a_x = & -r\dot{\beta}^2 - 2r\dot{\beta}\omega_y - r\omega_z^2 c_\beta^2 + 2r\Omega\omega_x s_\beta c_\beta \\
& + e_u R \ddot{\beta} c_{\beta_p} + e_u R \left(\dot{\beta}^2 + 2\dot{\beta}\omega_y \right) s_{\beta_p} - e_u R \omega_z^2 s_{\beta_T} c_\beta \\
& + 2 e_u R \Omega \omega_x s_{\beta_T} s_\beta - e_u R \left(\dot{p}_H s_\psi + \dot{q}_H c_\psi \right) c_{\beta_p}
\end{aligned} \tag{23a}
$$

$$
\begin{aligned}
a_y = & 2r\dot{\beta} \left(\omega_x c_\beta - \omega_z s_\beta \right) - r \left(\dot{p}_H c_\psi - \dot{q}_H s_\psi \right) s_\beta + r\dot{\omega}_z c_\beta \\
& + 2 e_u R \dot{\beta} \left(\omega_x s_{\beta_T} + \omega_z c_{\beta_T} \right) + e_u R \left(\dot{p}_H c_\psi - \dot{q}_H s_\psi \right) c_{\beta_T} \\
& + e_u R \dot{\omega}_z s_{\beta_T}
\end{aligned} \tag{23b}
$$

$$
\begin{aligned}
a_z = & -r\ddot{\beta} - r\omega_z^2 s_\beta c_\beta - 2r\Omega\omega_x c_\beta^2 + r \left(\dot{p}_H s_\psi + \dot{q}_H c_\psi \right) \\
& + e_u R \ddot{\beta} s_{\beta_p} - e_u R \left(\dot{\beta}^2 + 2\dot{\beta}\omega_y \right) c_{\beta_p} - e_u R \omega_z^2 s_{\beta_T} s_\beta \\
& - 2 e_u R \Omega \omega_x s_{\beta_T} c_\beta - e_u R \left(\dot{p}_H s_\psi + \dot{q}_H c_\psi \right) s_{\beta_p}
\end{aligned} \tag{23c}
$$

Like for the articulated rotor, the derivation of the equation above relies on the following assumptions:

1. The influence of the hub velocities is neglected such that $u_H \approx v_H \approx w_H \approx 0$.
2. The hub accelerations are also neglected, *i.e.*, $\dot{u}_H \approx \dot{v}_H \approx \dot{w}_H \approx 0$.
3. The products between lateral and longitudinal hub angular velocities in the rotating frame are considered to be small: $\omega_x^2 \approx \omega_y^2 \approx \omega_x\omega_y \approx 0$.
4. A simplification is made for the product between the longitudinal and vertical hub angular velocities in the rotating frame: $\omega_x\omega_z \approx -\Omega\omega_x$.
5. A similar simplification is made for the product between the lateral and vertical hub angular velocities in the rotating frame: $\omega_y\omega_z \approx -\Omega\omega_y$.

Rotor Forces and Moments

Aerodynamic Loads on Blade Elements Consider the geometry in Fig. 8, showing a section of a representative rotor blade moving through the air.

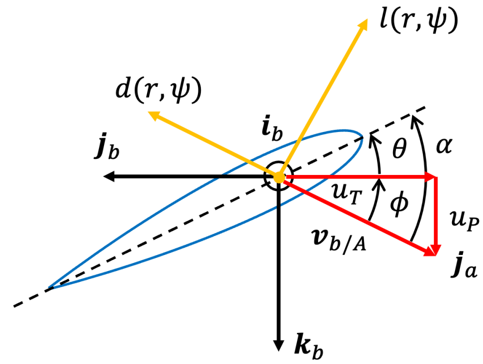

Figure 8: Section of a representative rotor blade element moving through the air.

Define the following quantities:
$\theta = \theta(r)$ is the geometric pitch of the blade,
$\phi = \phi(r)$ is the aerodynamic incidence angle,
α is the blade section angle of attack,
$\boldsymbol{v}_{b/a}$ is the velocity of the blade with respect to the air mass,
u_T is the velocity tangent to the blade leading edge ($-\boldsymbol{j}_b$ verse),
u_P is the velocity perpendicular to the $\boldsymbol{i}_b - \boldsymbol{j}_b$ plane ($\boldsymbol{k}_b$ verse), and
u_R is the velocity in the radial blade direction ($\boldsymbol{i}_b$ verse).

Note that u_p arises from the blade flapping motion, as well as from the rotorcraft vertical and angular motions; u_T arises mainly from the rotorcraft rotation and forward motion; and u_R arises mainly from the rotorcraft forward and lateral motion.

The velocity of the blade with respect to the air mass, expressed in blade-frame coordinates, is:

$$
\begin{aligned}
\boldsymbol{v}_{b/a}^b &= \boldsymbol{v}_{b/I}^b - \boldsymbol{v}_{a/I}^b \\
&= \boldsymbol{v}_{b/I}^b - \boldsymbol{T}_{H\to b} \boldsymbol{v}_{a/I}^H \\
&= \begin{bmatrix} u_b \\ v_b \\ w_b \end{bmatrix} - \boldsymbol{T}_{H\to b} \begin{bmatrix} 0 \\ 0 \\ v_i \end{bmatrix} = \begin{bmatrix} u_b + v_i s_\beta c_\zeta \\ v_b \\ w_b - v_i c_\beta \end{bmatrix} = \begin{bmatrix} u_R \\ -u_T \\ u_P \end{bmatrix}
\end{aligned} \tag{24}
$$

where $v_i = v_i(r,\psi) = \Omega R \lambda_i(r,\psi)$ is the induced velocity at the blade element. The geometric pitch of the blade is given by:

$$\theta(r,\psi) = \theta_P(\psi) + \theta_{\text{tw}}(r) + \beta \tan\delta_3 \tag{25}$$

where δ_3 is the pitch-flap coupling, θ_P represents the prescribed blade pitch at the root (from the pilot or control system), and θ_{tw} is the twist angle distribution. Here, $\theta_{\text{tw}} = 0$ at the root $r = 0$ and $\theta_{\text{tw}} < 0$ for $0 < r \leq R$. The blade pitch at the root is:

$$\theta_P(\psi) = \theta_0 + \theta_{1c}\cos\left(\psi - \Delta_{\text{sp}}\right) + \theta_{1s}\sin\left(\psi - \beta_T\Delta_{\text{sp}}\right) \tag{26}$$

where θ_0 is collective pitch, θ_{1c} is lateral cyclic, and θ_{1s} is longitudinal cyclic. Additionally, Δ_{sp} is the swashplate phasing angle. The total speed at the blade element is:

$$U_{\text{tot}} = \sqrt{u_R^2 + u_T^2 + u_P^2} \tag{27}$$

The velocity component in the plane of the blade section is:

$$U = \sqrt{u_T^2 + u_P^2} = \sqrt{u_T^2 \left(1 + \frac{u_P^2}{u_T^2}\right)} \tag{28}$$

The local angle of attack is:

$$\alpha = \theta + \phi = \theta + \tan^{-1}\left(\frac{u_P}{u_T}\right) \approx \theta + \frac{u_P}{u_T} \tag{29}$$

The local Mach number is:

$$M = \frac{U_{\text{tot}}}{v_{\text{sound}}} \tag{30}$$

where v_{sound} is the speed of sound. The local lift and drag coefficients are calculated in one of two ways. The first way is by using lookup tables of the airfoil section such that:

$$C_l = f(\alpha, M) \tag{31a}$$
$$C_d = f(\alpha, M) \tag{31b}$$

where C_l and C_d are the lift and drag coefficients. The second way is to assume linear lift variation of the angle of attack and constant drag coefficient, that is:

$$C_l \approx a_0 \alpha \tag{32a}$$
$$C_d \approx \delta \tag{32b}$$

where a_0 is the lift-curve slope (for a NACA 0012 airfoil at representative Mach numbers of order 10^6, $a_0 \approx 5.72$ 1/rad) and $\delta \approx 0.01$.

The sectional blade lift and drag are, expressed in the air mass frame, are:

$$l(r,\psi) = \frac{1}{2}\rho c(r) U^2 C_l \tag{33a}$$
$$d(r,\psi) = \frac{1}{2}\rho c(r) U^2 C_d \tag{33b}$$

where ρ is the air density and $c(r)$ is the blade chord. The blade segment forces, expressed in the RTP frame, are:

$$\begin{aligned}\begin{bmatrix} f_R \\ f_T \\ f_P \end{bmatrix} &= \boldsymbol{T}_{a \to RTP} \begin{bmatrix} 0 \\ -\frac{1}{2}\rho c(r) U^2 C_d \\ \frac{1}{2}\rho c(r) U^2 C_l \end{bmatrix} \\ &= \begin{bmatrix} 0 \\ \frac{1}{2}\rho c(r) U^2 \left(C_l \sin\phi - C_d \cos\phi\right) \\ \frac{1}{2}\rho c(r) U^2 \left(-C_l \cos\phi - C_d \sin\phi\right) \end{bmatrix}\end{aligned} \tag{34}$$

Assuming $u_P \ll u_T$ such that $U \approx u_T$ and $\tan^{-1}\left(\frac{u_P}{u_T}\right) \approx \frac{u_P}{u_T}$, the blade segment forces become:

$$f_R = 0 \tag{35a}$$

$$\begin{aligned} f_T &= \frac{1}{2}\rho c(r) u_T^2 \left[a_0 \left(\theta + \frac{u_P}{u_T}\right)\frac{u_P}{u_T} - \delta\right] \\ &= \frac{1}{2}\rho c(r) \left[a_0 \left(u_T \theta + u_P\right) u_P - u_T^2 \delta\right] \end{aligned} \tag{35b}$$

$$\begin{aligned} f_P &= \frac{1}{2}\rho c(r) u_T^2 \left[-a_0 \left(\theta + \frac{u_P}{u_T}\right) - \delta \overset{\approx 0}{\cancel{\frac{u_P}{u_T}}}\right] \\ &= -\frac{1}{2}\rho c(r) a_0 \left(u_T^2 \theta + u_P u_T\right) \end{aligned} \tag{35c}$$

Aerodynamic Forces and Moments About the Teetering Hinge The total blade aerodynamic loads, expressed in the RTP frame, are:

$$F_R = \int_0^R f_R(r) dr = 0 \tag{36a}$$

$$F_T = \int_0^R f_T(r) dr = \frac{1}{2}\rho a_0 \int_0^R c(r) \left[\left(\theta u_T - u_P\right) u_P - u_T^2 \delta\right] dr \tag{36b}$$

$$F_P = \int_0^R f_P(r) dr = -\frac{1}{2}\rho a_0 \int_0^R c(r) \left(u_T^2 \theta + u_P u_T\right) dr \tag{36c}$$

The total blade aerodynamic loads, expressed in teetering frame, are:

$$\begin{aligned} \boldsymbol{F}_{\text{aero}}^T &= \boldsymbol{T}_{b \to F} \boldsymbol{T}_{RTP \to b} \begin{bmatrix} F_R \\ F_T \\ F_P \end{bmatrix} \\ &= \begin{bmatrix} c_\beta & 0 & s_\beta \\ 0 & 1 & 0 \\ -s_\beta & 0 & c_\beta \end{bmatrix} \begin{bmatrix} 1 & 0 & 0 \\ 0 & -1 & 0 \\ 0 & 0 & 1 \end{bmatrix} \begin{bmatrix} F_R \\ F_T \\ F_P \end{bmatrix} \\ &= \begin{bmatrix} F_R c_{\beta_p} - F_P s_{\beta_p} \\ -F_T \\ F_R s_{\beta_p} + F_P s_{\beta_p} \end{bmatrix} = \begin{bmatrix} \left(F_x^T\right)_{\text{aero}} \\ \left(F_y^T\right)_{\text{aero}} \\ \left(F_z^T\right)_{\text{aero}} \end{bmatrix} \end{aligned} \tag{37}$$

The total aerodynamic moments about the teetering location, expressed in the blade frame, are:

$$\begin{aligned} \boldsymbol{M}_{\text{aero}}^b &= \int_0^R \boldsymbol{r}_{F \to P}^b \times \left(\boldsymbol{T}_{\text{RTP} \to b} \begin{bmatrix} f_R \\ f_T \\ f_P \end{bmatrix}\right) dr \\ &= \int_0^R \begin{bmatrix} r \\ 0 \\ 0 \end{bmatrix} \times \left(\begin{bmatrix} 1 & 0 & 0 \\ 0 & -1 & 0 \\ 0 & 0 & 1 \end{bmatrix} \begin{bmatrix} f_R \\ f_T \\ f_P \end{bmatrix}\right) dr \\ &= \int_0^R \begin{bmatrix} r \\ 0 \\ 0 \end{bmatrix} \times \begin{bmatrix} f_R \\ -f_T \\ f_P \end{bmatrix} dr \\ &= \int_0^R \begin{bmatrix} 0 \\ -r f_P \\ -r f_T \end{bmatrix} = \begin{bmatrix} \left(M_x^b\right)_{\text{aero}} \\ \left(M_y^b\right)_{\text{aero}} \\ \left(M_z^b\right)_{\text{aero}} \end{bmatrix} \end{aligned} \tag{38}$$

where the single components are:

$$\left(M_x^b\right)_{\text{aero}} = 0 \tag{39a}$$

$$\begin{aligned}\left(M_y^b\right)_{\text{aero}} &= -\int_0^R f_P(r) r dr \\ &= -\frac{1}{2}\rho a_0 \int_0^R c(r)\left(u_T^2\theta + u_P u_T\right) r dr\end{aligned} \tag{39b}$$

$$\begin{aligned}\left(M_z^b\right)_{\text{aero}} &= -\int_0^R f_T(r) r dr \\ &= -\frac{1}{2}\rho a_0 \int_0^R c(r)\left[\left(\theta u_T - u_P\right) u_P - u_T^2\delta\right] r dr\end{aligned} \tag{39c}$$

The aerodynamic moments about the teetering hinge, expressed in the teetering frame, are found as:

$$\begin{aligned}\boldsymbol{M}_{\text{aero}}^T =& \boldsymbol{T}_{b\to T}\boldsymbol{M}_{\text{aero}}^b + \boldsymbol{r}_{H\to T}^T \times \left(\boldsymbol{T}_{b\to T}\boldsymbol{F}_{\text{aero}}^b\right) \\ =& \begin{bmatrix} c_{\beta_p} & 0 & s_{\beta_p} \\ 0 & 1 & 0 \\ -s_{\beta_p} & 0 & c_{\beta_p}\end{bmatrix}\begin{bmatrix}\left(M_x^b\right)_{\text{aero}} \\ \left(M_y^b\right)_{\text{aero}} \\ \left(M_z^b\right)_{\text{aero}}\end{bmatrix} \\ &+ \begin{bmatrix}0 \\ 0 \\ e_u R\end{bmatrix} \times \left(\begin{bmatrix} c_{\beta_p} & 0 & s_{\beta_p} \\ 0 & 1 & 0 \\ -s_{\beta_p} & 0 & c_{\beta_p}\end{bmatrix}\begin{bmatrix}\left(F_x^b\right)_{\text{aero}} \\ \left(F_y^b\right)_{\text{aero}} \\ \left(F_z^b\right)_{\text{aero}}\end{bmatrix}\right) \\ =& \begin{bmatrix}\left(M_x^T\right)_{\text{aero}} \\ \left(M_y^T\right)_{\text{aero}} \\ \left(M_z^T\right)_{\text{aero}}\end{bmatrix}\end{aligned} \tag{40}$$

The total aerodynamic moments about the flapping hinge, expressed in hub frame components, are:

$$\left(\boldsymbol{M}_{b/F}^H\right)_{\text{aero}} = \boldsymbol{T}_{F\to H}\boldsymbol{T}_{T\to F}\left(\boldsymbol{M}_{b/F}^L\right)_{\text{aero}} = \begin{bmatrix}L_{\text{aero}} \\ M_{\text{aero}} \\ N_{\text{aero}}\end{bmatrix} \tag{41}$$

Then, the aerodynamic forces and moments coefficients are:

$$C_T = \frac{\sum_{i=1}^{N_b}\left(-F_{z_i}^F\right)_{\text{aero}}}{\pi\rho\Omega^2 R^4} \tag{42a}$$

$$C_L = \frac{\sum_{i=1}^{N_b}\left(L_i\right)_{\text{aero}}}{\pi\rho\Omega^2 R^5} \tag{42b}$$

$$C_M = \frac{\sum_{i=1}^{N_b}\left(M_i\right)_{\text{aero}}}{\pi\rho\Omega^2 R^5} \tag{42c}$$

where these quantities are used to drive the inflow dynamics.

Inertial Forces and Moments About the Undersling Location Like for the articulated rotor, the inertial forces are calculated by integrating the blade element acceleration along the span,

$$\begin{aligned}\boldsymbol{F}_{\text{inertial}}^b &= -\int_0^R m(r)\boldsymbol{a}_{P/I}^b(r) dr \\ &= -\int_0^R m(r)\begin{bmatrix}a_x \\ a_y \\ a_z\end{bmatrix} dr = \begin{bmatrix}\left(F_x^b\right)_{\text{inertial}} \\ \left(F_y^b\right)_{\text{inertial}} \\ \left(F_z^b\right)_{\text{inertial}}\end{bmatrix}\end{aligned} \tag{43}$$

with the exception that there is no flapping hinge. This results in the following inertial forces:

$$\begin{aligned}\left(F_x^b\right)_{\text{inertial}} =& -M_\beta\left[-\dot\beta^2 - 2\dot\beta\omega_y - \omega_z^2 c_\beta^2 + 2\omega\omega_x s_\beta c_\beta\right] \\ &- m_b e_u R\Big[\ddot\beta c_{\beta_p} + \left(\dot\beta^2 + \dot\beta\omega_y\right) s_{\beta_p} - \omega_z^2 s_{\beta_T} c_\beta \\ &+ 2\Omega\omega_x s_{\beta_T} s_\beta - \left(\dot p_H s_\psi + \dot q_H c_\psi\right) c_{\beta_p}\Big]\end{aligned} \tag{44a}$$

$$\begin{aligned}\left(F_y^b\right)_{\text{inertial}} =& -M_\beta\Big[2\dot\beta\left(\omega_x c_\beta - \omega_z s_\beta\right) - \left(\dot p_H c_\psi - \dot q_H s_\psi\right) s_\beta \\ &+ \dot\omega_z c_\beta\Big] - m_b e_u R\Big[2\dot\beta\left(\omega_x s_{\beta_T} + \omega_z c_{\beta_T}\right) \\ &+ \left(\dot p_H c_\psi - \dot q_H s_\psi\right) + \dot\omega_z s_{\beta_T}\Big]\end{aligned} \tag{44b}$$

$$\begin{aligned}\left(F_y^b\right)_{\text{inertial}} =& -M_\beta\Big[-\ddot\beta - \omega_z^2 s_\beta c_\beta - 2\Omega\omega_x c_\beta^2 \\ &+ \left(\dot p_H c_\psi + \dot q_H c_\psi\right)\Big] \\ &- m_b e_u R\Big[\ddot\beta s_{\beta_p} - \left(\dot\beta^2 + \dot\beta\omega_y\right) c_{\beta_p} \\ &- \omega_z^2 s_{\beta_T} s_\beta - 2\Omega\omega_x s_{\beta_T} c_\beta + \left(\dot p_H s_\psi + \dot q_H c_\psi\right) s_{\beta_p}\Big]\end{aligned} \tag{44c}$$

The inertia forces are transformed to the teetering frame via:

$$\begin{aligned}\boldsymbol{F}_{\text{inertial}}^T &= \boldsymbol{T}_{b\to T}\boldsymbol{F}_{\text{inertial}}^b \\ &= \begin{bmatrix} c_{\beta_p} & 0 & s_{\beta_p} \\ 0 & 1 & 0 \\ -s_{\beta_p} & 0 & c_{\beta_p}\end{bmatrix}\begin{bmatrix}\left(F_x^b\right)_{\text{inertial}} \\ \left(F_y^b\right)_{\text{inertial}} \\ \left(F_z^b\right)_{\text{inertial}}\end{bmatrix} = \begin{bmatrix}\left(F_x^T\right)_{\text{inertial}} \\ \left(F_y^T\right)_{\text{inertial}} \\ \left(F_z^T\right)_{\text{inertial}}\end{bmatrix}\end{aligned} \tag{45}$$

The inertial moments about the flapping hinge, expressed in the blade frame, are calculated as:

$$\begin{aligned}\boldsymbol{M}_{\text{inertial}}^b &= -\int_0^R \boldsymbol{r}_{F\to P}^b \times m(r)\boldsymbol{a}_{P/I}^b dr \\ &= -\int_0^R \begin{bmatrix}r \\ 0 \\ 0\end{bmatrix} \times \left(m(r)\begin{bmatrix}a_x \\ a_y \\ a_z\end{bmatrix}\right) dr \\ &= -\int_{eR}^R \begin{bmatrix}0 \\ -rm(r)a_z \\ rm(r)a_y\end{bmatrix} dr = \begin{bmatrix}\left(M_x^b\right)_{\text{inertial}} \\ \left(M_y^b\right)_{\text{inertial}} \\ \left(M_z^b\right)_{\text{inertial}}\end{bmatrix}\end{aligned} \tag{46}$$

resulting in:

$$\left(M_x^b\right)_{\text{inertial}} = 0 \tag{47a}$$

$$\begin{aligned}\left(M_y^b\right)_{\text{inertial}} =& I_\beta \left[-\ddot{\beta} - \omega_z^2 s_\beta c_\beta - 2\Omega\omega_x c_\beta^2 + \left(\dot{p}_H c_\psi + \dot{q}_H c_\psi\right)\right] \\ & M_\beta e_u R\Big[\ddot{\beta} s_{\beta_p} - \left(\dot{\beta}^2 + \dot{\beta}\omega_y\right) c_{\beta_p} - \omega_z^2 s_{\beta_T} s_\beta \\ & - 2\Omega\omega_x s_{\beta_T} c_\beta + \left(\dot{p}_H s_\psi + \dot{q}_H c_\psi\right) s_{\beta_p}\Big]\end{aligned} \tag{47b}$$

$$\begin{aligned}\left(M_y^b\right)_{\text{inertial}} =& -I_\beta \Big[2\dot{\beta}\left(\omega_x c_\beta - \omega_z s_\beta\right) - \left(\dot{p}_H c_\psi - \dot{q}_H s_\psi\right) s_\beta \\ & + \dot{\omega}_z c_\beta\Big] - M_\beta e_u R\Big[2\dot{\beta}\left(\omega_x s_{\beta_T} + \omega_z c_{\beta_T}\right) \\ & + \left(\dot{p}_H c_\psi - \dot{q}_H s_\psi\right) + \dot{\omega}_z s_{\beta_T}\Big]\end{aligned} \tag{47c}$$

Inertial Forces and Moments About the Teetering Hinge The inertial moments about the teetering hinge, expressed in the teetering frame, are found as:

$$\begin{aligned}\boldsymbol{M}^T_{\text{inertial}} =& \boldsymbol{T}_{b\to T}\boldsymbol{M}^b_{\text{inertial}} + \boldsymbol{r}^T_{H\to T} \times \left(\boldsymbol{T}_{b\to T}\boldsymbol{F}^b_{\text{inertial}}\right) \\ =& \begin{bmatrix} c_{\beta_p} & 0 & s_{\beta_p} \\ 0 & 1 & 0 \\ -s_{\beta_p} & 0 & c_{\beta_p}\end{bmatrix} \begin{bmatrix}\left(M_x^b\right)_{\text{inertial}} \\ \left(M_y^b\right)_{\text{inertial}} \\ \left(M_z^b\right)_{\text{inertial}}\end{bmatrix} \\ & + \begin{bmatrix}0 \\ 0 \\ e_u R\end{bmatrix} \times \left(\begin{bmatrix} c_{\beta_p} & 0 & s_{\beta_p} \\ 0 & 1 & 0 \\ -s_{\beta_p} & 0 & c_{\beta_p}\end{bmatrix} \begin{bmatrix}\left(F_x^b\right)_{\text{inertial}} \\ \left(F_y^b\right)_{\text{inertial}} \\ \left(F_z^b\right)_{\text{inertial}}\end{bmatrix}\right) \\ =& \begin{bmatrix}\left(M_x^T\right)_{\text{inertial}} \\ \left(M_y^T\right)_{\text{inertial}} \\ \left(M_z^T\right)_{\text{inertial}}\end{bmatrix}\end{aligned} \tag{48}$$

Total Forces and Moments about the Teetering Hinge The total forces at the teetering hinge, expressed in the teetering frame, are:

$$\boldsymbol{F}^T = \boldsymbol{F}^T_{\text{aero}} + \boldsymbol{F}^T_{\text{inertial}} = \begin{bmatrix}\left(F_x^T\right)_{\text{aero}} \\ \left(F_y^T\right)_{\text{aero}} \\ \left(F_z^T\right)_{\text{aero}}\end{bmatrix} + \begin{bmatrix}\left(F_x^T\right)_{\text{inertial}} \\ \left(F_y^T\right)_{\text{inertial}} \\ \left(F_z^T\right)_{\text{inertial}}\end{bmatrix} = \begin{bmatrix}F_x^T \\ F_y^T \\ F_z^T\end{bmatrix} \tag{49}$$

The total moments about teetering hinge, expressed in the teetering frame, are:

$$\begin{aligned}\boldsymbol{M}^T =& \boldsymbol{M}^T_{\text{aero}} + \boldsymbol{M}^T_{\text{inertial}} + \boldsymbol{M}^T_{\text{spring}} \\ =& \begin{bmatrix}\left(M_x^T\right)_{\text{aero}} \\ 0 \\ \left(M_z^T\right)_{\text{aero}}\end{bmatrix} + \begin{bmatrix}\left(M_x^T\right)_{\text{inertial}} \\ 0 \\ \left(M_z^T\right)_{\text{inertial}}\end{bmatrix} + \begin{bmatrix}0 \\ k_\beta \beta \\ 0\end{bmatrix} = \begin{bmatrix}M_x^T \\ M_y^T \\ M_z^T\end{bmatrix}\end{aligned} \tag{50}$$

where M_x is the torsional moment, M_y is moment through the flapping hinge, and M_z is the in-plane moment. Note that $M_y \neq 0$ only exists if there is a flapping spring (*i.e.*, $k_\beta \neq 0$), as no moments are transmitted through the flapping hinge. In the current study, no root spring is used.

Rotor Hub Forces and Moments The total forces acting at the flapping hinge of each blade can be summed to form the resultant forces at the rotor hub. These forces, expressed in the rotor hub frame are:

$$\begin{aligned}\boldsymbol{F}^H =& \sum_{i=1}^{N_b}\left(\boldsymbol{T}_{T\to H}\boldsymbol{F}_i^T\right) \\ =& \sum_{i=1}^{N_b}\left(\begin{bmatrix}-c_\psi c_{\beta_T} & -s_\psi & -c_\psi s_{\beta_T} \\ s_\psi c_{\beta_T} & -c_\psi & s_\psi s_{\beta_T} \\ -s_{\beta_T} & 0 & c_{\beta_T}\end{bmatrix}\begin{bmatrix}F_{x_i}^T \\ F_{y_i}^T \\ F_{z_i}^T\end{bmatrix}\right) \\ =& \begin{cases}\begin{bmatrix}X_H & Y_H & Z_H\end{bmatrix}^T, & \text{counterclockwise rotor} \\ \begin{bmatrix}X_H & -Y_H & Z_H\end{bmatrix}^T, & \text{clockwise rotor}\end{cases}\end{aligned} \tag{51}$$

The same can be done with the moments about each flapping hinge, such that the hub moments, expressed in the rotor hub frame are:

$$\begin{aligned}\boldsymbol{M}^H =& \sum_{i=1}^{N_b}\left\{\boldsymbol{T}_{T\to H}\left(\boldsymbol{M}_i^T + \boldsymbol{r}^T_{H\to T}\times\boldsymbol{F}_i^T\right)\right\} \\ =& \sum_{i=1}^{N_b}\left\{\boldsymbol{T}^T_{H\to T}\left(\boldsymbol{M}_i^T - \boldsymbol{F}_i^T\times\boldsymbol{r}^T_{H\to T}\right)\right\} \\ =& \sum_{i=1}^{N_b}\left\{\boldsymbol{T}^T_{H\to T}\left(\begin{bmatrix}M_{x_i}^T \\ M_{y_i}^T \\ M_{z_i}^T\end{bmatrix} - \begin{bmatrix}F_{x_i}^T \\ F_{y_i}^T \\ F_{z_i}^T\end{bmatrix}\times\begin{bmatrix}0 \\ 0 \\ e_u R\end{bmatrix}\right)\right\} \\ =& \sum_{i=1}^{N_b}\left\{\boldsymbol{T}^T_{H\to T}\begin{bmatrix}M_{x_i}^T - e_u R F_{y_i}^T \\ M_{y_i}^T + e_u R F_{x_i}^T \\ M_{z_i}^T\end{bmatrix}\right\} \\ =& \begin{cases}\begin{bmatrix}L_H & M_H & N_H\end{bmatrix}^T, & \text{counterclockwise rotor} \\ \begin{bmatrix}-L_H & M_H & -N_H\end{bmatrix}^T, & \text{clockwise rotor}\end{cases}\end{aligned} \tag{52}$$

The forces can be transformed to the body frame in the same manner as for an articulated rotor. Similarly, the moments can be resolved about the CG and then transformed to the body frame, following the same approach as in the articulated rotor case.

Flapping Dynamics

Individual Blade Coordinates By applying Newton's second law, *i.e.*, by performing a summation of the moments across both blades about the teetering hinge, one obtains:

$$\begin{aligned}0 =& \left(M_{y1}^T\right)_{\text{aero}} + \left(M_{y2}^T\right)_{\text{aero}} + \left(M_{y1}^T\right)_{\text{inertial}} + \left(M_{y2}^T\right)_{\text{inertial}} \\ & + \left(M_y^T\right)_{\text{spring}}\end{aligned} \tag{53}$$

This results in the following flapping dynamics about the teetering hinge:

$$\ddot{\beta}_T = -\left(\Omega^2 + \frac{k_\beta}{I_{\beta_T}}\right)\beta_T + 2\Omega\left(p_H\cos\psi - q_H\sin\psi\right) + \left(\dot{p}_H\sin\psi + \dot{q}_H\cos\psi\right) + \left[\frac{\left(M^T_{y_1}\right)_{\text{aero}} - \left(M^T_{y_2}\right)_{\text{aero}}}{I_{\beta_T}}\right] \tag{54}$$

where:

$$I_{\beta_T} = 2I_\beta\left(1 - \frac{2e_uRM_\beta\sin\beta_p}{I_\beta} + \frac{e_u^2R^2m_b}{I_\beta}\right) \tag{55}$$

is the total second mass moment about the teetering hinge. Here, I_β is the second mass moment of the blade, M_β is the first mass moment, and m_b is the blade mass. Note that the flapping dynamics equation above adopts the small angle approximations in the teetering angle. Additionally, the teetering angle is that of a reference blade, as the rotor is treated as a whole. This means that the teetering angle of one blade will be the opposite of that of the other blade, *i.e.*, $\beta_{T_2} = -\beta_{T_1}$.

Multi-Blade Coordinates Define an azimuthally averaged tip path plane to represent the rotor via β_{1c} and β_{1s}, such that the transformation from MBC to IBC is (Ref. 1):

$$\begin{bmatrix}\beta_{T_1}\\ \beta_{T_2}\end{bmatrix} = \begin{bmatrix}\cos\psi_1 & \sin\psi_1\\ \cos\psi_2 & \sin\psi_2\end{bmatrix}\begin{bmatrix}\beta_{1c}\\ \beta_{1s}\end{bmatrix} \tag{56}$$

The azimuthal position of the two rotor blades can be defined as:

$$\psi_i = \psi - \pi(i-1) \tag{57}$$

Substituting this equation in the equation above yields:

$$\begin{aligned}\begin{bmatrix}\beta_{T_1}\\ \beta_{T_2}\end{bmatrix} &= \underbrace{\begin{bmatrix}\cos\psi_1 & \sin\psi_1\\ \cos(\psi_1-\pi) & \sin(\psi_1-\pi)\end{bmatrix}}_{\boldsymbol{L}_\beta}\begin{bmatrix}\beta_{1c}\\ \beta_{1s}\end{bmatrix}\\ &= \begin{bmatrix}\cos\psi_1 & \sin\psi_1\\ -\cos\psi_1 & -\sin\psi_1\end{bmatrix}\begin{bmatrix}\beta_{1c}\\ \beta_{1s}\end{bmatrix}\\ &= \begin{bmatrix}\beta_{1s}\sin\psi_1 + \beta_{1c}\cos\psi_1\\ -\left(\beta_{1s}\sin\psi_1 + \beta_{1c}\cos\psi_1\right)\end{bmatrix}\end{aligned} \tag{58}$$

Thus, $\beta_{T_2} = -\beta_{T_1}$. Because these equations are redundant, a single teetering angle is chosen as $\beta_T = \beta_{T_1}$ and is defined as:

$$\beta_T = \beta_{1c}\cos\psi + \beta_{1s}\sin\psi \tag{59}$$

Consider now differentiating this equation:

$$\dot{\beta}_T = -\beta_{1c}\Omega\sin\psi + \beta_{1s}\Omega\cos\psi + \cancelto{0}{\dot{\beta}_{1c}\cos\psi + \dot{\beta}_{1s}\sin\psi} \tag{60}$$

where the following constraint was applied to drop the second term (Ref. 1):

$$\dot{\beta}_{1c}\cos\psi + \dot{\beta}_{1s}\sin\psi = 0 \tag{61}$$

Then, Eqs. (59) and (61) form a system of equations that, if inverted, leads to:

$$\begin{bmatrix}\beta_{1s}\\ \beta_{1c}\end{bmatrix} = \begin{bmatrix}\sin\psi\\ \cos\psi\end{bmatrix}\beta_T + \frac{1}{\Omega}\begin{bmatrix}\cos\psi\\ \sin\psi\end{bmatrix}\dot{\beta}_T \tag{62}$$

Differentiating the equation above yields:

$$\begin{aligned}\begin{bmatrix}\dot{\beta}_{1s}\\ \dot{\beta}_{1c}\end{bmatrix} &= \begin{bmatrix}\cancel{\dot{\beta}_T\sin\psi} + \Omega\beta_T\cos\psi + \frac{1}{\Omega}\ddot{\beta}_T\cos\psi - \cancel{\dot{\beta}_T\sin\psi}\\ \cancel{\dot{\beta}_T\cos\psi} - \Omega\beta_T\sin\psi - \frac{1}{\Omega}\ddot{\beta}_T\sin\psi - \cancel{\dot{\beta}_T\cos\psi}\end{bmatrix}\\ &= \Omega\begin{bmatrix}\cos\psi\\ -\sin\psi\end{bmatrix}\beta_T + \frac{1}{\Omega}\begin{bmatrix}\cos\psi\\ -\sin\psi\end{bmatrix}\ddot{\beta}_T\end{aligned} \tag{63}$$

which provides the flapping dynamics equations for a teetering rotor. Note that this is a first-order system in β_{1c} and β_{1s}, and it describes the teeter motion β_T for slow variations of β_{1c} and β_{1s}.

Inflow Dynamics

Rotor-on-rotor interactional inflow dynamics are modeled with the Combined Momentum Theory and Simple Vortex Theory (CMTSVT) (Refs. 12, 13). The inflow of the i^{th} rotor is expressed as the summation between the self-induced inflow of that rotor and the interference inflow from all other rotors:

$$\boldsymbol{\lambda}_i = \boldsymbol{\lambda}_{s_i} + \sum_{j=1, j\neq i}^{N}\boldsymbol{\lambda}_{\text{int}_{ij}} \tag{64}$$

where:

$\boldsymbol{\lambda}_i^T = [\lambda_{i_0}\ \lambda_{i_{1c}}\ \lambda_{i_{1s}}]$ is the total inflow of the i^{th} rotor in the local hub frame,

$\boldsymbol{\lambda}_{s_i}^T = \left[\lambda_{s_{i_0}}\ \lambda_{s_{i_{1c}}}\ \lambda_{s_{i_{1s}}}\right]$ is the self-induced inflow of the i^{th} rotor in the local hub frame, and

$\boldsymbol{\lambda}_{\text{int}_{ij}}^T = \left[\lambda_{\text{int}_{ij_0}}\ \lambda_{\text{int}_{ij_{1c}}}\ \lambda_{\text{int}_{ij_{1s}}}\right]$ is the interference inflow on the i^{th} from the j^{th} rotor in the i^{th} rotor hub frame.

The self-induced inflow dynamics of the i^{th} rotor are given by:

$$\dot{\boldsymbol{\lambda}}_{s_i} = \Omega\boldsymbol{T}_{W_i\to H_i}\boldsymbol{M}_{ii}^{-1}\left[-\boldsymbol{L}_{ii}^{-1}\left(\boldsymbol{T}_{H_i\to W_i}\boldsymbol{\lambda}_{s_i}\right) + \left(\boldsymbol{T}_{H_i\to W_i}\boldsymbol{F}_{ii}\right)\right] \tag{65}$$

where $\boldsymbol{M}_{ii}$ is the apparent mass matrix and $\boldsymbol{L}_{ii}$ is the static gain inflow matrix from Pitt-Peters (Ref. 14). Additionally, $\boldsymbol{F}_{ii}^T = [C_{T_i}\ -C_{M_i}\ -C_{L_i}]$, where C_{T_i}, C_{M_i}, and C_{L_i} are the thrust, pitching moments, and rolling moment coefficients of the i^{th} rotor in the local hub frame. The term $\boldsymbol{T}_{H_i\to W_i}$ corresponds to the transformation from the i^{th} rotor hub frame to the i^{th} rotor wind frame. The interference inflow on the i^{th} from the j^{th} rotor is given by:

$$\boldsymbol{\lambda}_{\text{int}_{ij}} = \eta_{ij}\boldsymbol{L}_{ij}\boldsymbol{\lambda}_{s_j} \tag{66}$$

where η_{ij} is a parameter that scales the non-dimensional quantities of the j^{th} rotor to non-dimensional quantities of the i^{th} rotor, and $\boldsymbol{L}_{ij}$ is the interference inflow matrix. More details can be found in (Refs. 9, 10, 12, 13).

FLIGHT DYNAMICS MODEL

Overview

The rotor model described above is integrated within an in-house MATLAB®/Simulink generic multi-rotor/wing flight dynamics and control code with the following characteristics:

- The aircraft fuselage is modeled as a rigid body. Fuselage aerodynamic forces are calculated either using equivalent flat-plate frontal, lateral, and vertical areas (Ref. 15), or through lookup tables.
- The user can specify any number of rotors and/or wings at arbitrary (and time-varying) orientations on the aircraft body.
- Wings accuracy level is selectable. The most complex model consists in wing-element theory. Rotor-on-wing aerodynamics inreractions are calculated based on the circulation at each wing element/panel using Biot-Savart and Hyeson (Ref. 16).
- The inflow dynamics can account for rotor-on-rotor interactional aerodynamics via Combined Momentum Theory and Simple Vortex Theory (CMTSVT) (Refs. 9, 10, 12, 13).
- The model is implemented in MATLAB® to ease the design and testing of flight control laws.
- The model is integrated with a baseline control law based on Dynamic Inversion (Refs. 17–20) with inner-attitude and outer-velocity control loops.

This simulation model was validated against RASCAL JUH-60 (Ref. 21) and XV-15 (Refs. 18, 20) flight-test data for rotors with flap-only dynamics, as well as against small-scale quad-, hexa-, and octo-copters with no flapping dynamics (Ref. 21). A simulation model is developed for the ultralight coaxial helicopter. The geometry of this vehicle is shown in trimmed flight at hover and 80 kts in Fig. 9. Note that, for illustration purposes, both rotorcraft adopt a ROBIN fuselage (Refs. 22, 23). The general characteristics of the aircraft are listed in Table 1. The simulation model adopts NACA23012 airfoils for the rotors and the empennage.

Table 1: General characteristics of the CoAX 2D ultralight helicopter.

Parameter	Value	Units
Mass and inertia		
Gross weight, W	992	lb
Roll moment of inertia, I_{xx}	446	sl-ft^2
Pitch moment of inertia, I_{yy}	848	sl-ft^2
Yaw moment of inertia, I_{zz}	629	sl-ft^2
Roll/yaw product of inertia, I_{xz}	129	sl-ft^2
CG fuselage station	0	ft
CG butt line	0	ft
CG water line	0	ft
Fuselage		
Frontal drag area	14.16	ft^2
Sideward drag area	53.64	ft^2
Vertical drag area	50.04	ft^2
Fuselage station	0	ft
Butt line	0	ft
Water line	0	ft
Rotors		
Number of blades	2	-
Radius	10.66	ft
Mean blade chord	0.72	ft
Undersling	0.2	ft
Precone	1.85	deg
Blade twist	-7.65	deg
Blade weight	17.64	lb
Blade first mass moment	3.4	sl-ft
Blade second mass moment	17.72	sl-ft^2
Angular speed	47.65	rad/s
Tilt Angle	-4	deg
Fuselage station	0.13	ft
Butt line	0	ft
Water line	$\{2.38, 4.52\}$	ft
Horizontal Stabilizer		
Span	4.15	ft
Mean chord	0.82	ft
Fuselage station (aero center)	9.35	ft
Butt line (aero center)	0	ft
Water line (aero center)	0	ft
Vertical Stabilizer		
Span	4.0	ft
Mean chord	1.20	ft
Fuselage station (aero center)	1.15	ft
Butt line (aero center)	0	ft
Water line (aero center)	0.33	ft

Nonlinear Dynamics

The rotorcraft flight dynamics are formulated as a nonlinear time-periodic system:

$$\dot{\boldsymbol{x}} = \boldsymbol{f}(\boldsymbol{x}, \boldsymbol{u}, t) \tag{67a}$$

$$\boldsymbol{y} = \boldsymbol{g}(\boldsymbol{x}, \boldsymbol{u}, t) \tag{67b}$$

where $\boldsymbol{x} \in \mathbb{R}^n$ is the state vector, $\boldsymbol{u} \in \mathbb{R}^m$ is the control input vector, $\boldsymbol{y} \in \mathbb{R}^l$ is the output vector, and t is the dimensional time in seconds. It is convenient to note that dimensional time can be related to the azimuth angle ψ of a reference blade, also known as non-dimensional time, via the following relation: $\psi = \Omega t$, where Ω is the angular speed, in rad/s, of the slowest rotor. It follows that the fundamental period of the system is $T = (2\pi)/\Omega$ seconds, which corresponds to 2π radians or one

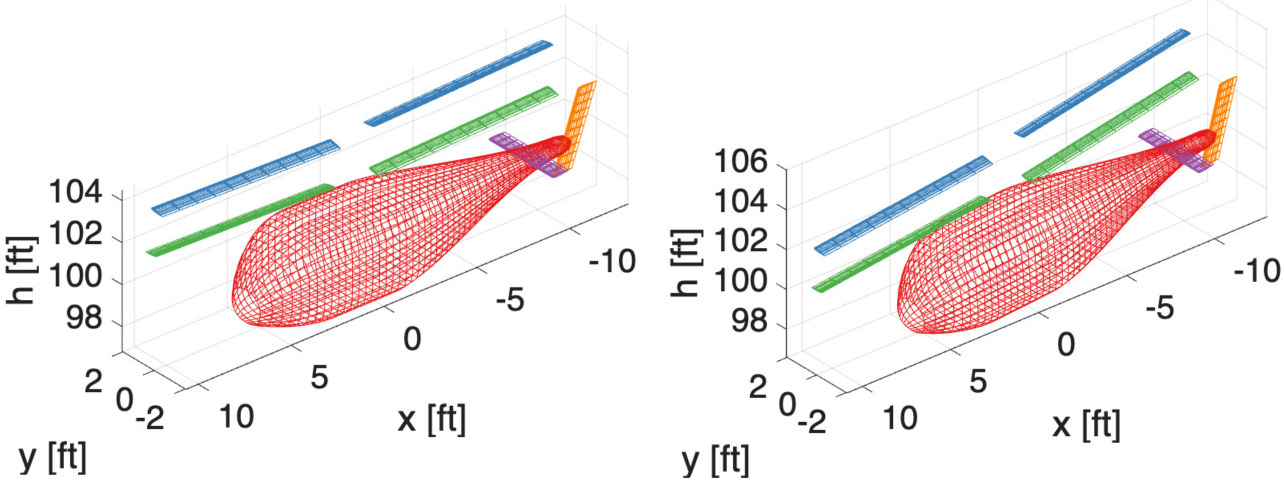

(a) Hover.

(b) 80 kts.

Figure 9: Ultralight coaxial helicopter aircraft geometry at hover and 80 kts forward flight.

revolution of the slowest rotor. The nonlinear functions $\boldsymbol{f}$ and $\boldsymbol{g}$ are T-periodic in time such that:

$$\boldsymbol{f}(\boldsymbol{x},\boldsymbol{u},t) = \boldsymbol{f}(\boldsymbol{x},\boldsymbol{u},t+T) \tag{68a}$$

$$\boldsymbol{g}(\boldsymbol{x},\boldsymbol{u},t) = \boldsymbol{g}(\boldsymbol{x},\boldsymbol{u},t+T) \tag{68b}$$

The state vector is:

$$\boldsymbol{x}^T = \left[\boldsymbol{x}_{\text{RB}}^T \; \boldsymbol{x}_{\text{R}_1}^T \; \cdots \; \boldsymbol{x}_{\text{R}_{n_\text{R}}}^T\right] \tag{69}$$

where $\boldsymbol{x}_{\text{RB}}$ are the rigid-body states and $\boldsymbol{x}_{\text{R}_i}$ are the states of the i^{th} of n_R rotors. The rigid-body state vector is common to all aircraft and is given by:

$$\boldsymbol{x}_{\text{RB}}^T = [u \; v \; w \; p \; q \; r \; \phi \; \theta \; \psi \; x \; y \; z] \tag{70}$$

where:

u, v, w are the longitudinal, lateral, and vertical velocities in the body-fixed frame,

p, q, r are the roll, pitch, and yaw rates,

ϕ, θ, ψ are the Euler angles, and

x, y, z are the positions in the North-East-Down (NED) frame.

The general form of the i^{th} rotor state vector is:

$$\boldsymbol{x}_{\text{R}_i}^T = \left[\boldsymbol{\beta}_\text{M}^T \; \dot{\boldsymbol{\beta}}_\text{M}^T \; \boldsymbol{\lambda}_\text{s}^T \; \boldsymbol{\lambda}^T \; \Omega_\text{R} \; \psi_\text{R}\right] \tag{71}$$

where:

$\boldsymbol{\beta}_\text{M}$ are the flapping angles in multi-blade coordinates,

$\boldsymbol{\lambda}_\text{s}^T = [\lambda_{\text{s}_0} \; \lambda_{\text{s}_{1c}} \; \lambda_{\text{s}_{1s}}]$ is a vector containing the self-induced dynamic inflow components,

$\boldsymbol{\lambda}^T = [\lambda_0 \; \lambda_{1c} \; \lambda_{1s}]$ is a vector containing the total dynamic inflow components,

Ω_R is the rotor angular speed, and

ψ_R is the azimuth angle of a reference blade.

The pilot input vector is:

$$\boldsymbol{u}^T = \left[\delta_{\text{lat}} \; \delta_{\text{lon}} \; \delta_{\text{col}} \; \delta_{\text{ped}}\right] \tag{72}$$

where:

δ_{lat} and δ_{lon} are the lateral and longitudinal stick positions,

δ_{col} is the collective stick position, and

δ_{ped} is the pedals position.

The pilot inputs are converted to actuator commands via a mixing matrix, in which each pilot input maps directly to a corresponding rotor input. This simplified approach was adopted due to the lack of publicly available information on the CoAX 2D's mechanical mixing system. The control effector inputs are:

$$\boldsymbol{u}_\text{C} = \boldsymbol{u}_\text{R} \tag{73}$$

where $\boldsymbol{u}_\text{R}$ are the rotor actuator inputs. The actuator inputs for the i^{th} rotor are:

$$\boldsymbol{u}_{\text{R}_i}^T = [\theta_0 \; \theta_{1c} \; \theta_{1s} \; \Omega_{\text{cmd}}] \tag{74}$$

where:

θ_0 θ_{1s} θ_{1c} are the collective, longitudinal cyclic, and lateral cyclic swashplate inputs, and

Ω_{cmd} is the commanded rotor speed.

Trim, Linearization, and Model Order Reduction

Linearized, time-invariant models are obtained by trimming the rotorcraft flight dynamics at a desired flight conditions via the periodic trim algorithm of Ref. 24, 25. Subsequently, the rotorcraft flight dynamics are linearized about each trim point via perturbation methods by only retaining the averaged (or zeroth) dynamics. To eliminate the need to measure or estimate states associated with the higher-order dynamics, where the higher-order dynamics include rotor and higher harmonic dynamics, it is desirable to reduce the order of the linearized dynamics. This is a necessary step to make linearized models tractable for practical control design purposes. This can be achieved through residualization, a portion of singular perturbation theory that pertains to LTI systems (Ref. 26). Application of residualization to the rotorcraft flight dynamics can be found in several published research studies, *e.g.*, Refs. 17, 18, 20, 27–30.

Flight Control Design

The flight control architecture chosen for this study is Nonlinear Dynamic Inversion (NDI). Application of NDI control laws to rotorcraft can be found in Refs. 9, 19, 25, 27, 29–38. A key aspect of Dynamic Inversion (DI) is the reliance on model inversion to cancel the plant dynamics and track a desired reference model. One convenient feature of Nonlinear Dynamic Inversion (NDI) is that it inverts the plant model within its feedback linearization loop. Compared to other conventional model-following control strategies, such as Explicit Model Following (EMF), this approach reduces the explicit need for gain scheduling of the control law. However, the plant model used for feedback linearization still requires scheduling with the flight condition, as variations in aircraft dynamics must be accounted for. Additionally, the feedback gains may need to be scheduled in cases where consistent disturbance rejection (measured in disturbance rejection bandwidth) and robustness performance (measured in broken-loop crossover frequency) must be maintained across the flight envelope.

A multi-loop NDI control law based on Refs. 9, 17, 20, 25, 31, 32 is designed to enable automatic flight in low-speed flight, cruise flight, and transition between the two. The schematic of the closed-loop rotorcraft dynamics is shown in Fig. 10. The outer loop controller, shown in Fig. 11 tracks longitudinal, lateral, and vertical ground velocities commands in the heading frame and calculates the desired pitch and roll attitudes for the inner loop to track, in addition to the collective control input setting. The desired response type for the outer loop is Translational Rate Command (TRC). The inner loop, shown in Fig. 12 achieves stability, disturbance rejection, and desired response characteristics about the roll, pitch, yaw, and heave axes. The inner loop uses Attitude Command / Attitude Hold (ACAH) response is used for the roll and pitch axes, whereas Rate Command / Direction Hold (RCDH) is used for the yaw axis.

Because the rotorcraft flight envelope includes low-speed flight (*i.e.*, lower than approximately 50 kts) as well as high-speed flight (*i.e.*, greater than 50 kts), different control strategies are necessary to control the yaw rate for these two flight conditions. Above 50 kts, turn coordination is used; below 50 kts, no turn coordination (Ref. 39) is used. These control strategies are summarized as follows:

$$\phi'_{\text{cmd}} = \begin{cases} \phi_{\text{cmd}}, & V < V_{\text{HS}} \\ \tan^{-1}\left(\dfrac{V}{g}\psi_{\text{cmd}}\right), & V \geq V_{\text{HS}} \end{cases} \tag{75}$$

where $V_{\text{HS}} = 50$ kts.

RESULTS

Trim

As a first step, the simulation models are trimmed at incremental flight speeds from 0 to 90 knots (the maximum reported speed for the CoAX 2D), both with and without rotor-on-rotor interactions. The trim strategy assumes zero sideslip – that is, the nose is aligned with the relative wind. Figure 13 shows the trim Euler angles as a function of increasing flight speed. While the trim roll and yaw attitudes remain zero in the case without rotor-on-rotor interactions, the bank angle is nonzero when these interactions are included, particularly at speeds between 0 and 40 knots. This behavior arises because, with rotor-on-rotor interactions active, the lower rotor operates in the wake of the upper rotor and therefore requires more power to produce the same thrust – or, equivalently, produces less thrust for a given power input. As a result, the aircraft cannot be trimmed at both zero sideslip and zero roll attitude simultaneously. Although this outcome confirms that the proposed model captures the physical effect appropriately, the practical implications are minimal, as the resulting roll attitude remains well below 1 degree.

The thrust and power for each rotor, both with and without rotor-on-rotor aerodynamic interactions, are summarized in Table 2. When aerodynamic interactions are off, both rotors exhibit identical inflow values, with self-induced inflow (λ_{s_0}) and total inflow (λ_0) equal at 0.034, reflecting independent rotor operation without influence from the other rotor's wake. When aerodynamic interactions are on, differences emerge due to the coaxial configuration where the lower rotor operates in the wake of the upper rotor. Notably, the lower rotor's total inflow ($\lambda_0 = 0.075$) is higher than that of the upper rotor ($\lambda_0 = 0.056$), indicating the additional induced velocity from the upper rotor's slipstream. In contrast, its self-induced inflow ($\lambda_{s_0} = 0.031$) is lower than that of the upper rotor ($\lambda s_0 = 0.036$). This reduction is consistent with the rotor effectively operating in an axial climb condition, where a portion of the induced inflow is provided externally by the upper rotor's downwash rather than being self-generated (Ref. 15). Regarding thrust, rotor-on-rotor aerodynamic interactions cause a clear redistribution of loads between the rotors. When interactions are off, each rotor generates equal thrust (494.8 lb), consistent with a symmetric, non-interacting coaxial configuration. When interactions are on, however, the upper rotor produces significantly more thrust (567.6 lb) than the lower rotor (422.0 lb). This imbalance arises from the lower rotor operating in the wake of the upper rotor, which alters the local inflow conditions and reduces its effective thrust-producing capability for the same power or torque, and when torque balance is required for trim. This is reflected in the power required by each rotor under interactions is equal ($37.74hp$), substantially higher than the no-interaction power (23.08 hp each). The power coefficients (C_P) are also equal at 0.00019 with interactions, compared to 0.00011 without, indicating a marked increase in power consumption due to aerodynamic coupling. These results demonstrate that rotor-on-rotor aerodynamic interactions in coaxial configurations significantly affect the trim inflow distribution, thrust sharing, and power requirements of each rotor. These findings are consistent with prior results reported in the literature (Refs. 9, 10).

Figure 14 shows the trim pilot stick inputs as a function of

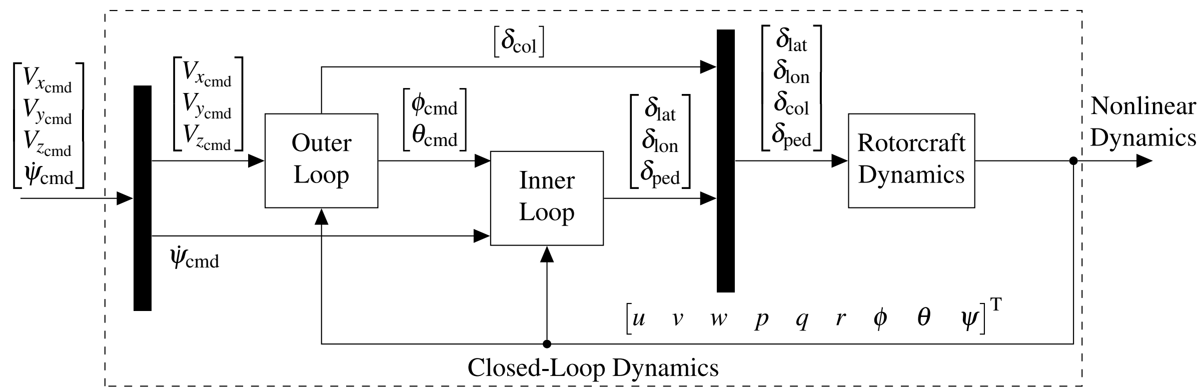

Figure 10: Schematic of the closed-loop rotorcraft dynamics.

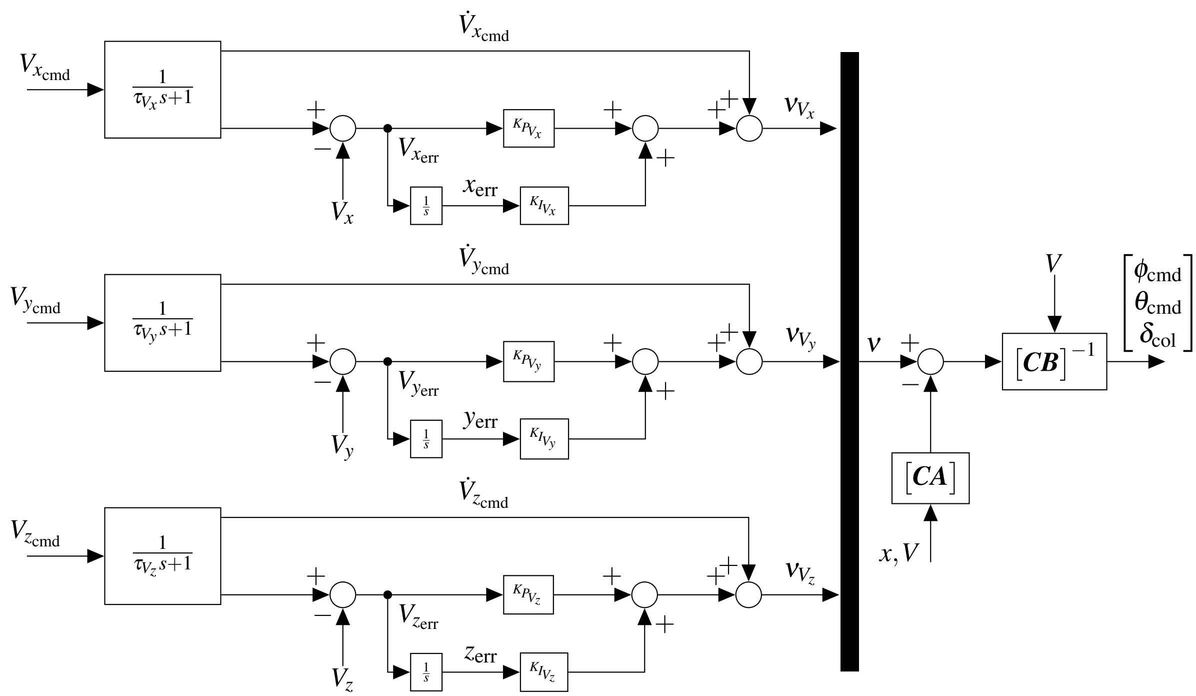

Figure 11: Dynamic inversion outer-velocity control loop.

increasing airspeed. In this figure, longitudinal stick inputs are nearly identical for cases with and without rotor-on-rotor aerodynamic interactions. However, lateral stick, collective, and pedal inputs differ. Lateral stick inputs are slightly higher when interactions are included, while collective inputs are significantly higher – particularly below 50 kts. This is due to the lower rotor operating in the wake of the upper rotor, which reduces its effective thrust for the same power input, thereby requiring greater collective input to maintain trim. This effect diminishes with increasing airspeed as the wake skew angle increases, causing less of the upper rotor's wake to impinge on the lower rotor. Above 50 kts, the effect becomes negligible. Differences in pedal inputs arise because the rotors do not exactly torque-balance each other in hover and low-speed flight, again due to the lower rotor being affected by the wake of the upper rotor. These discrepancies in yaw control inputs also diminish above 20 kts and are negligible beyond 50 kts. In summary, rotor-on-rotor interactions affect not only trim power and thrust sharing but also pilot control inputs required to maintain trim across the flight envelope.

Stability and Response Characteristics

The flight dynamics trimmed at hover are linearized using perturbation methods (Ref. 24) and subsequently residualized to assess the effects of interactional dynamics on the rigid-body modes. Figure 15 shows the eigenvalues of the residualized dynamics with and without rotor-on-rotor aerodynamic interactions, alongside the flight-identified eigenvalues from Refs. 2, 3. The eigenvalues of the linearized models – both with interactions on and off – exhibit the classic hovering cubic eigenstructure (Ref. 4), in which the lateral and longitudinal dynamics feature one stable, relatively high-frequency real mode and a complex pair of unstable, low-frequency oscil-

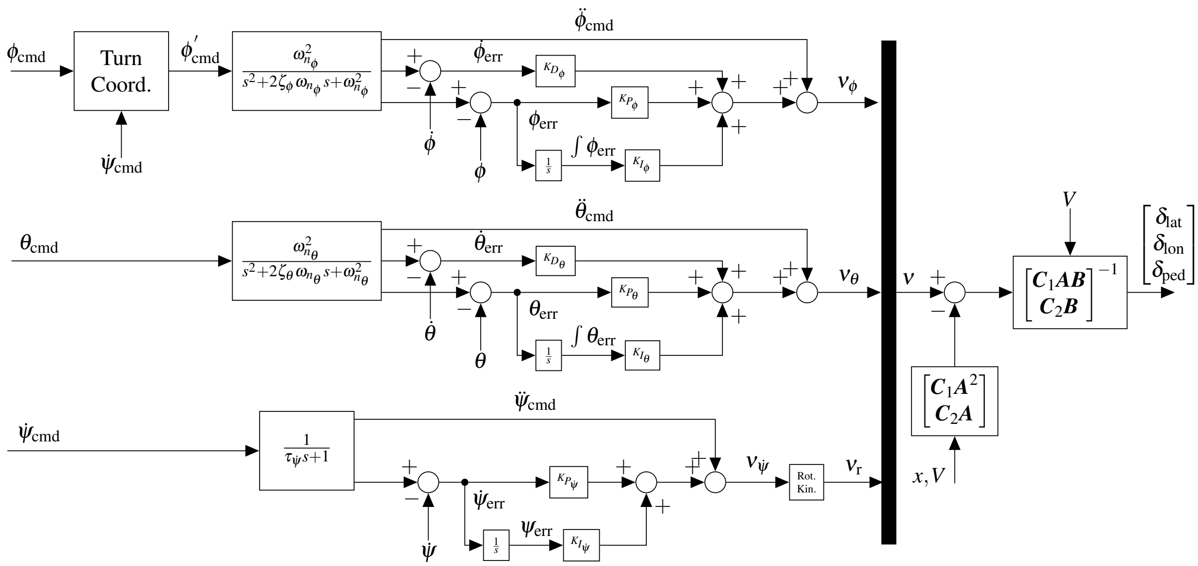

Figure 12: Dynamic inversion inner-attitude control loop.

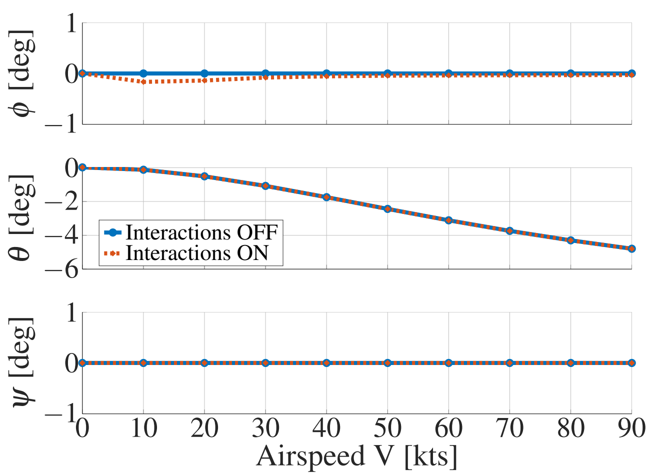

Figure 13: Trim Euler angles for increasing speed.

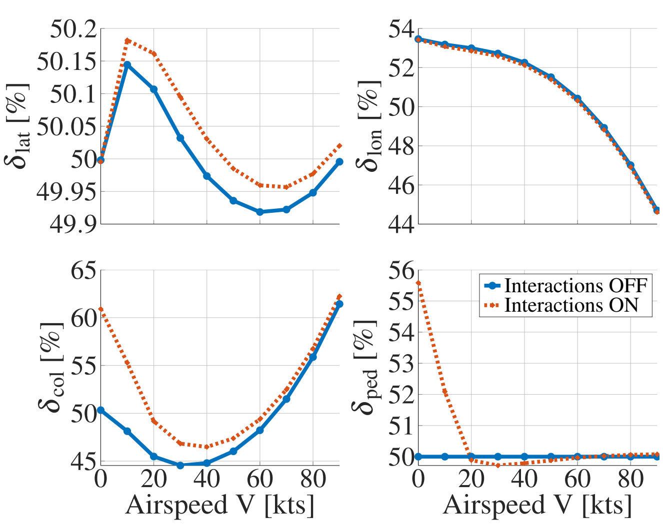

Figure 14: Trim pilot stick inputs for increasing speed.

Table 2: Hover performance of counter-rotating coaxial rotors, with and without rotor-on-rotor aerodynamic interactions.

Variable	Interactions	Rotor 1 (Upper)	Rotor 2 (Lower)	Units
λ_0	On	0.056	0.075	–
	Off	0.034	0.034	–
λ_{1s}	On	0.000	0.001	–
	Off	0.000	0.000	–
λ_{1c}	On	0.000	0.000	–
	Off	0.000	0.000	–
λ_{s_0}	On	0.036	0.031	–
	Off	0.034	0.034	–
$\lambda_{s_{1s}}$	On	0.000	0.001	–
	Off	0.000	0.000	–
$\lambda_{s_{1c}}$	On	0.000	0.000	–
	Off	0.000	0.000	–
T	On	567.6	422.0	lb
	Off	494.8	494.8	lb
C_T	On	0.00259	0.00193	–
	Off	0.00226	0.00226	–
P	On	37.44	37.44	hp
	Off	23.08	23.08	hp
C_P	On	0.00019	0.00019	–
	Off	0.00011	0.00011	–
Ω	On	261.3	261.3	rad/s
	Off	261.3	261.3	rad/s

latory modes. In addition, two subsidence modes are present, characterized by real negative eigenvalues near the imaginary axis. The primary difference between the interactions-on and interactions-off cases, though modest, lies in a slightly higher natural frequency of the unstable roll and pitch oscillation modes when interactions are included. When compared with the flight-identified eigenvalues from Refs. 2, 3, the model predictions are generally in good agreement. The main discrepancy is that the physics-based model predicts the unstable roll and oscillatory modes at higher natural frequencies. A second difference is that the physics-based model predicts a coupled, oscillatory pitch and heave subsidence, whereas these modes are decoupled and exhibit real eigenvalues in the flight data. It is important to note that the linearized models correspond to the coupled lateral-directional and longitudinal-heave dynamics, whereas the eigenvalues reported in Refs. 2, 3 are based on decoupled, flight-identified models. This may partially explain the mismatch. Additionally, the pilot's weight – non-negligible relative to the aircraft weight – can affect the center of gravity. In this study, the center of gravity is assumed to lie below the rotor system, but its actual location during the flight tests is unknown and may have introduced further discrepancies. Overall, the eigenvalues predicted by the physics-based model are reasonably close to those obtained from system identification.

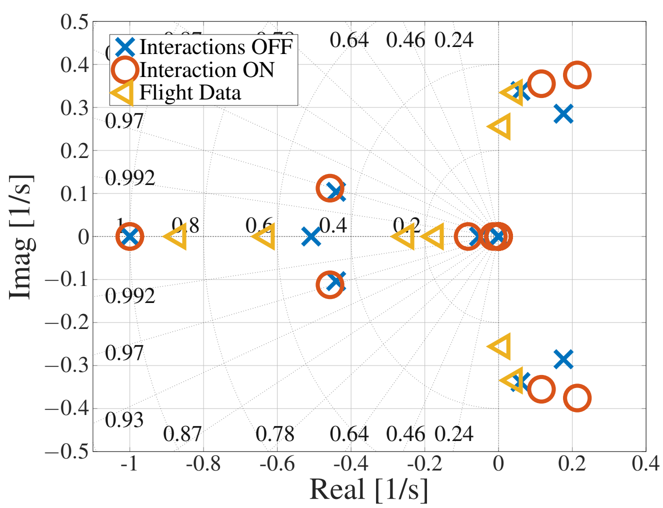

Figure 15: Eigenvalues of the residualized dynamics with and without rotor-on-rotor dynamics and the eigenvalues of the flight-identified model of (Refs. 2, 3).

To gain further insight into how rotor-on-rotor interactional aerodynamics affect hover flight dynamics, on-axis frequency responses are computed using the full-order dynamics with and without interactions. Figure 16 presents the resulting frequency responses. Rotor-on-rotor interactions primarily influence the magnitude of the roll, yaw, and heave-axis responses, with the no-interaction case exhibiting lower magnitude. The higher magnitude in the presence of rotor-on-rotor interactions leads to improved agreement with flight-identified responses, particularly at frequencies above approximately 0.4–0.5 rad/s. It is worth noting, however, that as indicated by the eigenvalue analysis, the mismatch in the unstable oscillatory roll mode causes a peak response at a slightly higher frequency than observed in the flight-identified data. Rotor-on-rotor interactions also appear to affect the phase, especially in the heave-axis response, bringing it closer to the flight-identified behavior. These trends are consistent with prior studies (Refs. 10, 40). Overall, the agreement between the physics-based model and the flight-identified frequency responses is good – especially when rotor-on-rotor interactions are included.

Closed-Loop Simulation

The rotorcraft flight dynamics are linearized and residualized at each discrete speed increment to obtain the dynamic inversion (DI) control law coefficient matrices. The resulting DI control laws are evaluated in closed-loop simulations of a 30-second acceleration from hover to cruise flight, during which the rotorcraft performs a right turn while climbing at 300 ft/min. This maneuver, shown in Fig. 17, illustrates the performance of the flight control laws in the lateral axis. The rotorcraft begins in a hover condition and starts accelerating at the forth second of the simulation, as shown in Fig. 17a. Climb begins later, at the ninth second, also at 300 ft/min (see Fig. 17a). At approximately fourteen seconds, the rotorcraft initiates a right turn with a yaw rate of $\dot{\psi} = 0.15$ rad/s. Since the rotorcraft is accelerating, and the bank angle required for coordinated turn is given by $\phi = \tan^{-1}\left(\frac{\dot{\psi}V}{g}\right)$, the increasing airspeed V leads to a corresponding increase in bank angle ϕ during the turn. The resulting steady increase in heading is shown in Fig. 17b. The turn is maintained until 20 seconds, while the acceleration ends at 27 seconds. The climb rate, however, is maintained for the duration of the simulation. The outer velocity loop is shown to track the commanded velocities accurately, with minimal off-axis response. Similarly, the inner attitude loop closely tracks the roll, pitch, and yaw attitudes commanded by the outer loop, also with minimal cross-axis coupling. In conclusion, the automatic flight control system effectively tracks the desired commands with minimal off-axis response, even during a complex maneuver involving simultaneous commands along three axes.

CONCLUSIONS

This paper described the theoretical derivation, implementation, and validation of a teetering rotor model for application in flight dynamics simulations. The rotor formulation was generic and accounted for both positive and negative angular rotor speeds. The module was integrated within a generic multi-rotor/wing flight dynamics code implemented in MATLAB®/Simulink. The model was validated against flight-identified data for an ultralight coaxial helicopter. The impact of rotor-on-rotor interactional aerodynamics was evaluated in trimmed flight using spectral and frequency response analyses. Model-order reduction methods were investigated to support the development of linearized models that were tractable for flight control design while still capturing the effects of rotor-on-rotor interactions on the vehicle flight dynamics. Model-following flight control laws based on these reduced-order linearized models were developed and tested on the nonlinear dynamics. Based on this work, the following conclusions can be reached:

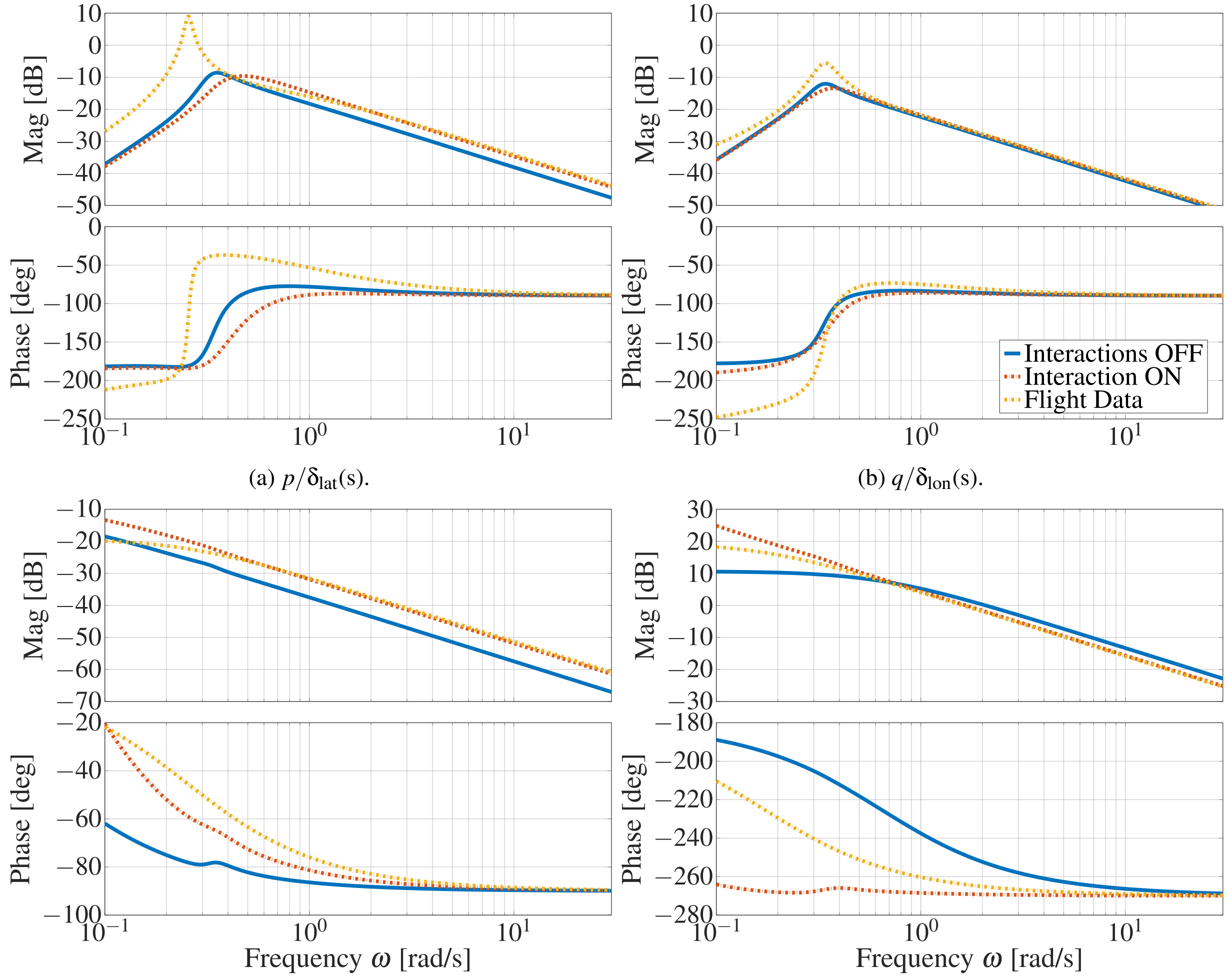

(a) $p/\delta_{\mathrm{lat}}(s)$.

(b) $q/\delta_{\mathrm{lon}}(s)$.

(c) $r/\delta_{\mathrm{ped}}(s)$.

(d) $w/\delta_{\mathrm{col}}(s)$.

Figure 16: On-axis frequency responses in hover of the full-order dynamics with and without rotor-on-rotor interactions and of the flight-identified models of (Refs. 2, 3).

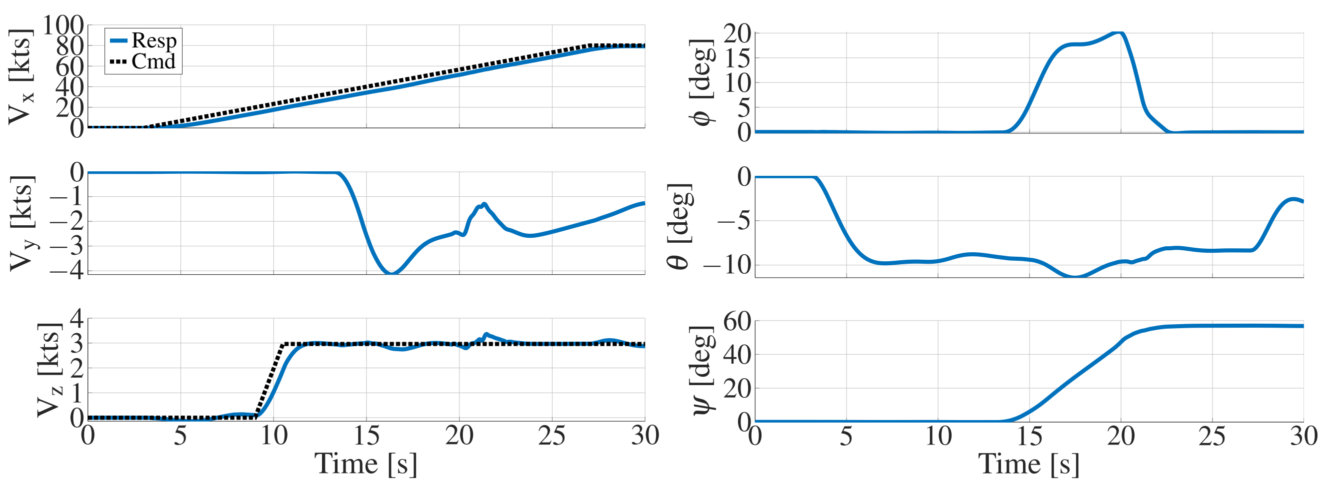

(a) Heading-frame velocities.

(b) Euler angles.

Figure 17: Transition from hover to high-speed forward flight.

1. Inclusion of rotor-on-rotor aerodynamic interactions introduces nonzero roll trim attitudes and increases in collective and pedal input demands – especially below 50 knots – due to asymmetric thrust sharing between the up-

per and lower rotors.

2. Rotor-on-rotor interactions lead to higher thrust and self-induced inflow on the upper rotor and lower thrust on the lower rotor, despite equal power consumption. This reflects the lower rotor operating in the induced wake of the upper rotor, increasing total power requirements by over 60%.

3. Including rotor-on-rotor aerodynamic interactions increases the gain in roll, yaw, and heave frequency responses – particularly above 0.4–0.5 rad/s – bringing the model into closer agreement with flight-identified data. Phase alignment also improves, especially in the heave response, where the interactions help replicate the phase lag observed in flight. The mismatch in the natural frequency of the unstable oscillatory roll mode may stem from uncertainty in the lateral center-of-gravity location during the flight tests used for parametric identification.

4. The dynamic inversion control system, developed using residualized dynamics that account for rotor-on-rotor aerodynamic interactions, performs reliably across a range of flight maneuvers, including coordinated turns, vertical climb, and longitudinal acceleration. The inner-loop controllers provide consistent attitude and rate tracking, while the outer-loop controllers track velocity commands with limited cross-axis coupling.

Author contact:

U. Saetti:	saetti@umd.edu
T. Kreienkamp:	st160623@stud.uni-stuttgart.de
S. Özkurt:	sueleyman.oezkurt@ifr.uni-stuttgart.de
W. Fichter:	fichter@ifr.uni-stuttgart.de

ACKNOWLEDGMENTS

The authors would like to thank Benjamin Rothaupt for his valuable support in providing detailed vehicle property data essential to the development and validation of the simulation model.

REFERENCES

1. Johnson, W., *Rotorcraft Aeromechanics*, Cambridge University Press, 2013. DOI: https://doi.org/10.1017/CBO9781139235655.

2. Richter, T., Rothaupt, B., Steinwandel, A., Fichter, W., and Grebing, B., "Stability Augmentation System for Coaxial Ultralight Helicopters," Proceedings of the 76th Annual Forum of the Vertical Flight Society, Virtual, October 2020. DOI: https://doi.org/10.4050/F-0076-2020-16426.

3. Richter, T., Rothaupt, B., , Fichter, W., and Grebing, B., "System Identification of a Coaxial Ultralight Helicopter," Proceedings of the 76th Annual Forum of the Vertical Flight Society, Virtual, October 2020. DOI: https://doi.org/10.4050/F-0076-2020-16288.

4. McRuer, D. T., Ashkenas, I. L., and Graham, D., *Aircraft Dynamics and Automatic Control*, Princeton University Press, 1973, Chapter 6.

5. Hosseini, B., Sax, F., Rhein, J., Holzapfel, F., Maier, L., Barth, A., Hajek, M., and Grebing, B., "Global Model Identification for a Coaxial Helicopter," Proceedings of the 78th Annual Forum of the Vertical Flight Society, Fort Worth, TX, May 10-12, 2022. DOI: https://doi.org/10.4050/F-0078-2022-17575.

6. Hosseini, B., Mbikayi, Z., Bachfischer, M., Holzapfel, F., and Rauleder, J., "Simulation, Flight Dynamics, and Control Design for a Coaxial Rotorcraft," Proceedings of the AIAA SciTech 2024 Forum, Orlando, FL, 2024. DOI: https://doi.org/10.2514/6.2024-1717.

7. Bachelder, E. N., and Godfroy-Cooper, M., "Real-Time Dynamic Inflow Model for a Coaxial Helicopter Configuration Using the Lattice–Boltzmann Method," AIAA 2024-1718, AIAA SciTech Forum, Orlando, FL, Jan 8–12, 2025. DOI: https://doi.org/10.2514/6.2024-1718.

8. Hosseini, B., Grauer, J. A., Holzapfel, F., and Rauleder, J., "Higher-Order System Identification and Control Design for a Coaxial Rotorcraft," *Journal of Aircraft,* Article in Advance, 2021. DOI: https://doi.org/10.2514/1.C038157.

9. Saetti, U., and Guner, F., "Interactional Aerodynamics Modeling and Flight Control Design of Multi-Rotor Aircraft," Proceedings of the 6th Decennial VFS Aeromechanics Specialists' Conference, Santa Clara, CA, Feb 6-8, 2024.

10. Jun, C. A., D., Saetti, U., and Juhasz, O., "Flight Dynamics of a Coaxial Compound Helicopter with Rotor-On-Rotor Interactional Aerodynamics," Proceedings of the 50th European Rotorcraft Forum, Marseille, France, Sep 10–12, 2024.

11. "EDM Aerotec GmbH Webpage," https://www.edm-aerotec.de/, Accessed: 2025-02-24.

12. Guner, F., and Prasad, J. V. R., "Combined Momentum Theory and Simple Vortex Theory Inflow Model for Multirotor Configurations," *Journal of the American Helicopter Society*, Vol. 67, (2), 2022, pp. 1–15. DOI: https://doi.org/10.4050/JAHS.67.022007.

13. Guner, F., "A Multirotor Inflow Model Based on Combined Momentum Theory and Simple Vortex Theory (CMTSVT) for Flight Simulations," Proceedings of the 78th Annual Forum of the Vertical Flight Society, Fort Worth, TX, May 10-12, 2022.

14. Pitt, D. M., and Peters, D. A., "Theoretical Prediction of Dynamic-Inflow Derivatives," Proceedings of the 6th European Rotorcraft and Powered Lift Aircraft Forum, Bristol, England, Sep 16-19, 1980.

15. Leishman, J. G., *Principles of Helicopter Aerodynamics*, Cambridge University Press, 2006.

16. Hyeson, H. H., "Equations for the Induced Velocities Near a Lifting Rotor with Nonuniform Azimuthwise Vorticity Distribution," Technical report, NASA TN D-394, 1960.

17. Horn, J. F., "Non-Linear Dynamic Inversion Control Design for Rotorcraft," *Aerospace*, Vol. 6, (38), 2019. DOI: https://doi.org/10.3390/aerospace6030038.

18. Saetti, U., and Bugday, B., "Tiltrotor Simulations with Coupled Flight Dynamics, State-Space Aeromechanics, and Aeroacoustics," *Journal of the American Helicopter Society*, **69**, 012003 (2024). DOI: https://doi.org/10.4050/JAHS.69.012003.

19. Saetti, U., Horn, J. F., Lakhmani, S., Lagoa, C., and Berger, T., "Design of Dynamic Inversion and Explicit Model Following Control Laws for Quadrotor UAS," *Journal of the American Helicopter Society*, **65**, 032006 (2020). DOI: https://doi.org/10.4050/JAHS.65.032006.

20. Saetti, U., "Dynamic Inversion Flight Control Laws for Automatic Transition of Tilt-Rotor/Wing Aircraft," *Journal of the American Helicopter Society*, **65**, 032005 (2025). DOI: https://doi.org/10.4050/JAHS.70.032005.

21. Saetti, U., Rinaldi, M., Guglieri, G., Berger, T., and Lu, L., "Identification of Control-Equivalent Turbulence Input (CETI) Models from Rotorcraft Simulations," Proceedings of the 81$^{\text{th}}$ Annual Forum of the Vertical Flight Society, Virginia Beach, VA, May 20–22, 2025. DOI: https://doi.org/10.4050/F-0081-2025-81.

22. Mineck, R. E., and Gorton, S. A., "Steady and Periodic Pressure Measurements on a Generic Helicopter Fuselage Model in the Presence of a Rotor," Technical report, NACA TM-2000-210286, 2000.

23. Hillier, B. B., Stock, M. J., and Gharakhan, "Robust and Corrected Coefficients for the ROtor-Body-INteraction Body," *AIAA Journal*, Vol. 59, (10), 2021, pp. 4281–4283. DOI: https://doi.org/10.2514/1.J060303.

24. Saetti, U., and Rogers, J. D., "Revisited Harmonic Balance Trim Solution Method for Periodically-Forced Flight Vehicles," *Journal of Guidance, Control, and Dynamics*, Vol. 44, (5), May 2021, pp. 1008–1017. DOI: https://doi.org/10.2514/1.G005553.

25. Saetti, U., Horn, J. F., and Brentner, K. S., "Linearized Models of the Coupled Rotorcraft Flight Dynamics and Acoustics for Real-Time Noise Prediction," *Journal of the American Helicopter Society*, Vol. 69, (2), 2024. DOI: https://doi.org/10.4050/JAHS.69.022002.

26. Kokotovic, P. V., O'Malley, R. E., and Sannuti, P., "Singular Perturbations and Order Reduction in Control Theory, an Overview," *Automatica*, Vol. 12, (2), 1976, pp. 123–132. DOI: 10.1016/0005-1098(76)90076-5.

27. Saetti, E. J., U., , and Horn, J. F., "Flight Dynamics and Control of an eVTOL Concept Aircraft with a Propeller-Driven Rotor," *Journal of the American Helicopter Society*, Vol. 67, (3), 2022, pp. 153–166. DOI: https://doi.org/10.4050/JAHS.67.032012.

28. Saetti, U., and Horn, J. F., "Implementation and Linearization of State-Space Free-Vortex Wake Models for Rotary- and Flapping-Wing Vehicles," *Journal of the American Helicopter Society*, Vol. 68, (4), Apr 2023, pp. 42004–42017. DOI: 10.4050/JAHS.68.042004.

29. Saetti, U., Rogers, J. D., Alam, M., and Jump, M., "Tau Theory-Based Flare Control in Autonomous Helicopter Autorotation," *Aerospace*, Vol. 33, (1), 2024. DOI: https://doi.org/10.3390/aerospace11010033.

30. Saetti, U., Horn, J. F., and Berger, T., "On the Effects of Rotor Induced Vibrational Stability on Helicopter Flight Dynamics," *CEAS Aeronautical Journal,* Article in Advance, 2024. DOI: https://doi.org/10.1007/s13272-024-00718-w.

31. Berger, T., Tischler, M. B., and Horn, J. F., "Outer-Loop Control Design and Simulation Handling Qualities Assessment for a Coaxial-Compound Helicopter and Tiltrotor," Proceedings of the 77$^{\text{th}}$ Annual Forum of the Vertical Flight Society, Virtual, Oct 5-8, 2020. DOI: 10.4050/F-0076-2020-16392.

32. Berger, T., Tischler, M. B., and Horn, J. F., "High-Speed Rotorcraft Pitch Axis Response Type Investigation," Proceedings of the 77$^{\text{th}}$ Annual Forum of the Vertical Flight Society, Virtual, May 10-14, 2021. DOI: 10.4050/F-0077-2021-16793.

33. Sahani, N. A., and Horn, J. F., "Adaptive Model Inversion Control of a Helicopter with Structural Load Limiting," *Journal of Guidance, Control, and Dynamics*, Vol. 29, (2), 2006, pp. 411–420. DOI: https://doi.org/10.2514/1.13391.

34. Theron, J. P., Horn, J. F., Wachspress, D. A., and Enciu, J., "Nonlinear dynamic inversion control for urban air mobility aircraft with distributed electric propulsion," Proceedings of the 76$^{\text{th}}$ Annual Forum of the Vertical Flight Society, October 5–8, 2020. DOI: https://doi.org/10.4050/F-0076-2020-16396.

35. Walter, A., Mckay, M., Niemiec, R., Gandhi, F., and Berger, T., "Hover Dynamics and Flight Control of a UAM-Scale Quadcopter With Hybrid RPM and Collective Pitch Control," *Journal of the American Helicopter Society*, **68**, 022012 (2023), pp. 143–160(18). DOI: https://doi.org/10.4050/JAHS.68.022012.

36. Enciu, J., Horn, J. F., and Langelaan, J. W., "Formation Control of a Rotorcraft Multilift System," *Journal of the American Helicopter Society*, **62**, 042011 (2022). DOI: https://doi.org/10.4050/JAHS.62.042011.

37. Spires, J. M., and Horn, J. F., "Multi-Input Multi-Output Model-Following Control Design Methods for Rotorcraft," *Journal of the American Helicopter Society*, **66**, 032002 (2021), pp. 1–15(15). DOI: https://doi.org/10.4050/JAHS.66.032002.

38. Scaramal, M., and Horn, J. F., "Load Alleviation on Compound Rotorcraft Using Load Feedback and Extremum Seeking Control," *Journal of Guidance, Control, and Dynamics*, Vol. 46, (12), 2023. DOI: https://doi.org/10.2514/1.G007192.

39. Blakelock, J. H., *Automatic Control of Aircraft and Missiles*, John Wiley & Sons, 1965. DOI: 10.1017/S0001924000057912.

40. Hersey, S., Celi, R., Tischler, M. B., Juhasz, O., Rand, O., and Khromov, V., "State-Space Inflow Model Identification and Flight Dynamics Coupling for an Advanced Coaxial Rotorcraft Configuration," Proceedings of the 73rd Annual Forum of the Vertical Flight Society, May 9-11, 2017.

CLASSIFICATION & COPYRIGHT

The paper must be unclassified for release to the public and cleared by the appropriate company and/or government agency if necessary. CEAS and its national member societies shall be allowed to publish the paper. The copyright information is stat-ed on the Forum website https://www.rotorcraft-forum.eu/ and on the front page of this template. All papers presented at the ERF will be published as ERF proceedings. In addition, they will be available in a freely accessible web-based repository 2 years after the respective conference.

APPENDIX

The residualized flight dynamics system matrix at hover, for the case including rotor-on-rotor interactions, is:

$$\boldsymbol{A}_{0\text{ kts}} = \begin{bmatrix} -0.0079 & 0.0098 & 0.0014 & 0.2365 & 0.6854 & 0.0287 & 0 & -32.1700 \\ 0.0045 & -0.0099 & 0.0007 & -0.3045 & -0.0294 & -0.0154 & 32.1700 & 0.0000 \\ -0.0639 & 0.0021 & -0.0172 & -0.0150 & 0.3094 & 0.1049 & 0.0015 & -0.0084 \\ -0.0014 & -0.0013 & -0.0008 & -0.1126 & 0.1021 & -0.0225 & 0 & 0 \\ 0.0005 & -0.0014 & -0.0003 & -0.0653 & -0.0957 & -0.0056 & 0 & 0 \\ 0.0006 & 0.0004 & -0.0036 & -0.0201 & 0.0139 & -0.0946 & 0 & 0 \\ 0 & 0 & 0 & 1.0000 & -0.0000 & 0.0003 & 0.0000 & 0.0000 \\ 0 & 0 & 0 & 0 & 1.0000 & 0.0000 & -0.0000 & 0 \end{bmatrix}$$

The control matrix corresponding to pilot stick inputs at hover is:

$$\boldsymbol{B}_{0\text{ kts}} = \begin{bmatrix} 0.0194 & -0.6596 & -0.0004 & 0.0000 \\ 0.2363 & 0.0001 & -0.0001 & 0.0000 \\ -0.0015 & -0.0631 & -1.6552 & 0.3480 \\ 0.1839 & 0.0006 & -0.0002 & 0.0049 \\ -0.0014 & 0.0814 & 0.0001 & 0.0000 \\ 0.0379 & 0.0014 & -0.0009 & 0.0256 \\ 0 & 0 & 0 & 0 \\ 0 & 0 & 0 & 0 \end{bmatrix}$$

The state and control input vectors corresponding to the above system and control matrices are:

$$\boldsymbol{x}^T = [u\ v\ w\ p\ q\ r\ \phi\ \theta]$$

$$\boldsymbol{u}^T = \left[\delta_{\text{lat}}\ \delta_{\text{lon}}\ \delta_{\text{col}}\ \delta_{\text{ped}}\right] \tag{76}$$

where u, v, and w are in units of ft/s; p, q, and r are in rad/s; and ϕ and θ are in radians. Additionally, the mixing matrix to convert pilot stick inputs to swashplate inputs is:

$$\begin{bmatrix} \theta_{0_{R_1}} \\ \theta_{1c_{R_1}} \\ \theta_{1s_{R_1}} \\ \theta_{0_{R_2}} \\ \theta_{1c_{R_2}} \\ \theta_{1s_{R_2}} \end{bmatrix} = \begin{bmatrix} 0 & 0 & \frac{1}{2} & -\frac{2}{9} \\ 5 & 0 & 0 & 0 \\ 0 & 2 & 0 & 0 \\ 0 & 0 & \frac{1}{2} & 0 \\ 5 & 0 & 0 & 0 \\ 0 & 2 & 0 & 0 \end{bmatrix} \begin{bmatrix} \delta_{\text{lat}} \\ \delta_{\text{lon}} \\ \delta_{\text{col}} \\ \delta_{\text{ped}} \end{bmatrix}$$

The system and control matrices at 80 kts forward flight are:

$$\boldsymbol{A}_{80\text{ kts}} = \begin{bmatrix} -0.0764 & -0.0000 & 0.0569 & -0.0032 & 8.7042 & 0.0041 & 0 & -32.1016 \\ -0.0003 & -0.0983 & 0.0008 & -8.4619 & 0.0021 & -117.2804 & 32.1016 & -0.0013 \\ 0.0478 & -0.0002 & -1.5518 & 0.0773 & 117.1017 & 0.0140 & 0.0199 & 2.0971 \\ 0.0002 & 0.0107 & 0.0009 & -0.2150 & 0.0491 & -0.1385 & 0 & 0 \\ 0.0031 & 0.0002 & -0.0322 & -0.0308 & -0.3888 & -0.0065 & 0 & 0 \\ 0.0000 & 0.0357 & 0.0005 & -0.1600 & 0.0065 & -0.4482 & 0 & 0 \\ 0 & 0 & 0 & 1.0000 & 0.0000 & -0.0653 & -0.0000 & -0.0000 \\ 0 & 0 & 0 & 0 & 1.0000 & 0.0006 & 0.0000 & 0 \end{bmatrix}$$

$$\boldsymbol{B}_{80\text{ kts}} = \begin{bmatrix} 0.0238 & -0.3477 & 0.1617 & -0.0356 \\ 0.0045 & 0.0046 & 0.0031 & -0.0013 \\ -0.1717 & -4.0453 & -2.8214 & 0.6238 \\ 0.1343 & 0.0018 & -0.0006 & 0.0039 \\ -0.0021 & 0.0412 & -0.0190 & 0.0060 \\ 0.0276 & 0.0006 & -0.0001 & 0.0204 \\ 0 & 0 & 0 & 0 \\ 0 & 0 & 0 & 0 \end{bmatrix}$$